



<https://theses.gla.ac.uk/>

Theses Digitisation:

<https://www.gla.ac.uk/myglasgow/research/enlighten/theses/digitisation/>

This is a digitised version of the original print thesis.

Copyright and moral rights for this work are retained by the author

A copy can be downloaded for personal non-commercial research or study,  
without prior permission or charge

This work cannot be reproduced or quoted extensively from without first  
obtaining permission in writing from the author

The content must not be changed in any way or sold commercially in any  
format or medium without the formal permission of the author

When referring to this work, full bibliographic details including the author,  
title, awarding institution and date of the thesis must be given

Enlighten: Theses

<https://theses.gla.ac.uk/>  
[research-enlighten@glasgow.ac.uk](mailto:research-enlighten@glasgow.ac.uk)

# A Proton Detector for Medium Energy Physics

Jörg Andreas Gregel

Presented as a Thesis for the Degree of Master of Science by research

Department of Physics and Astronomy,  
University of Glasgow,  
August 1995.

©J.A. Gregel, 1995.

ProQuest Number: 10992191

All rights reserved

INFORMATION TO ALL USERS

The quality of this reproduction is dependent upon the quality of the copy submitted.

In the unlikely event that the author did not send a complete manuscript and there are missing pages, these will be noted. Also, if material had to be removed, a note will indicate the deletion.



ProQuest 10992191

Published by ProQuest LLC (2018). Copyright of the Dissertation is held by the Author.

All rights reserved.

This work is protected against unauthorized copying under Title 17, United States Code  
Microform Edition © ProQuest LLC.

ProQuest LLC.  
789 East Eisenhower Parkway  
P.O. Box 1346  
Ann Arbor, MI 48106 – 1346

*Thesis*  
10208  
*Copy 1*

GLASGOW  
UNIVERSITY  
LIBRARY

## Abstract

This thesis is concerned with a proton detector matrix used in a measurement of the  $^{12}\text{C}(\gamma, p\gamma)^{11}\text{B}$  reaction. The matrix consists of 20 CsI(Tl) crystals, each of which is read out by a photodiode.

Chapter 1 gives an introduction into the physics of the experiment and explains the aim and execution of this experiment.

Chapter 2 is a description of the detector composition including the electronics.

Chapter 3 contains measurements which have been made in order to obtain optimum energy resolution and uniform light collection efficiency for the detector.

Chapter 4 describes some Monte Carlo models. These models are investigations into the light collection efficiencies for different crystal and diode sizes and the proton detection characteristics.

Chapter 5 gives a description of the setup used in the  $^{12}\text{C}(\gamma, p\gamma)^{11}\text{B}$  experiment. It also presents some preliminary results of this experiment.

## **Declaration**

The work presented in this thesis was carried out at the University of Glasgow and at the MAXLAB, University of Lund (Sweden) between October 1994 and September 1995. I participated fully in the execution of all the work described. This thesis was composed by myself.

**Jörg Gregel**

## Acknowledgements

I want to express my gratitude to the Erlangen Professors D.K. Breitingner (Inorg.Chemistry), H.M. Hofmann (Theor.Physics) and G. Ritter (Exp.Physics) for providing expert opinions for the German Academic Exchange Service (DAAD). Without financial subsistence by the DAAD, the completion of this M.Sc. project would have been unthinkable. Also acknowledged is the receipt of a small amount of money by means of a Stephenson Exchange Scholarship.

On the Scottish side I am grateful to Professor Owens for accepting me on as an M.Sc. student at the University of Glasgow and to John Annand for being my supervisor. Thanks are also due to members of the Glasgow University Nuclear Physics group (in alphabetical order): Rebecca Crawford, Sam Hall, Peter Harty, David Ireland, Annemarie Keenan, Scott Lumsden, Cameron McGeorge and Robin Watson.

Apart from the hard Scottish winter, it was a pleasure to work in this group and the insight into British academic and social life was an interesting experience.

# Contents

<b>1</b>	<b>Introduction - The <math>^{12}\text{C}(\gamma, p\gamma')^{11}\text{B}</math> Experiment</b>	<b>2</b>
<b>2</b>	<b>The Proton Detector</b>	<b>10</b>
2.1	Scintillation Material . . . . .	11
2.2	Mechanical Construction . . . . .	13
2.3	Electronics for the CsI(Tl) Scintillation Readout . . . . .	15
<b>3</b>	<b>Measurements</b>	<b>20</b>
3.1	Optimization of the Setup . . . . .	21
3.2	Effects of varying the reflective wrapping on the light collection efficiency and the signal-to-noise ratio. . . . .	30
3.3	Uniformity Measurements. . . . .	32
<b>4</b>	<b>Monte Carlo Simulations</b>	<b>37</b>
4.1	Simulation of the Light Collection Efficiency . . . . .	38
4.1.1	Description of the models . . . . .	38
4.1.2	Results . . . . .	42

4.2	Simulation of the Proton Detection . . . . .	45
4.2.1	Effect and Importance of Proton-Nuclei-Interactions . . .	45
4.2.2	Performance of the Detection System . . . . .	48
<b>5</b>	<b>Test of the Proton Detector</b>	<b>54</b>
5.1	Experimental Setup . . . . .	55
5.1.1	Tagged Photons . . . . .	56
5.1.2	Target . . . . .	58
5.1.3	Electronics . . . . .	58
5.2	Missing Energy Spectra . . . . .	60
5.3	Preliminary Results . . . . .	64
5.4	Conclusion . . . . .	70
<b>A</b>	<b>The Bethe-Bloch Equation</b>	<b>71</b>
<b>B</b>	<b>Generation of Non-Uniform Probability Distributions</b>	<b>74</b>

# List of Figures

1.1	<i>Total photon absorption cross section in <math>{}^9\text{Be}</math></i>	4
1.2	<i>Excited states in <math>{}^{11}\text{B}</math></i>	8
2.1	<i><math>\Delta E, E</math> scatter-plot obtained in the <math>{}^{12}\text{C}(\gamma, p\gamma){}^{11}\text{B}</math> test run in Lund</i>	15
2.2	<i>Schematic diagram of the <math>\Delta E, E</math> telescope in a typical experimental geometry</i>	16
2.3	<i>Input and output circuit of one channel of the HQV800 series</i>	18
2.4	<i>A simplified diagram of the shaping amplifier</i>	19
3.1	<i>Test experimental setup</i>	22
3.2	<i>Capacitance and leakage current for the PIN-Diodes employed in the present work.</i>	24
3.3	<i>Measured leakage currents of the diodes at room temperature in light-tight boxes</i>	25
3.4	<i>Reverse voltage dependence of the noise. Shaping time <math>3\mu\text{s}</math>. The error bars are due to the measurement of the leakage current.</i>	26
3.5	<i>Fitting and Subtracting the background.</i>	27

3.6	<i>Resolution for different reverse voltages . . . . .</i>	28
3.7	<i>Shaping time dependence of the noise. . . . .</i>	29
3.8	<i>Resolution and light output vs. number of teflon layers . . . . .</i>	31
3.9	<i>Setup for uniformity measurements . . . . .</i>	33
3.10	<i>Visualization of the Geometry . . . . .</i>	34
3.11	<i>Position dependence of the light output . . . . .</i>	36
4.1	<i>Reflectance function for CsI. . . . .</i>	40
4.2	<i>Illustration of the procedure to obtain the new direction of the reflected photon. . . . .</i>	41
4.3	<i>Paradoxical Situation . . . . .</i>	42
4.4	<i>Light collection efficiency for generation of scintillation quanta in different crystal regions. . . . .</i>	44
4.5	<i>Calculated percentage of nuclear interactions with varying proton energy in CsI . . . . .</i>	47
4.6	<i>Detector components considered in the present Simulation . . . . .</i>	48
4.7	<i>Energy losses of 40 MeV protons in various detector components</i>	49
4.8	<i>Proton kinetic energy dependent energy loss in the <math>\Delta E</math> detectors, aluminium and teflon - Simulation . . . . .</i>	51
4.9	<i>Energy losses of 300 MeV muons in the 20 CsI(Tl) blocks - Sim- ulation . . . . .</i>	52

4.10	<i>Energy losses of cosmic ray muons in the 20 CsI(Tl) blocks - Experiment . . . . .</i>	53
5.1	<i>The MAX accelerator in Lund (Sweden). . . . .</i>	55
5.2	<i>Schematic diagram of the tagging technique . . . . .</i>	57
5.3	<i>Schematic diagram. Electronics for signal processing related to the proton detection system. . . . .</i>	59
5.4	<i>Typical TDC spectrum after scatter-plot proton identification and a rough timing cut . . . . .</i>	64
5.5	<i><math>^{12}\text{C}</math> missing energy spectrum. Target thickness <math>118\text{ mg}\cdot\text{cm}^{-2}</math>. Preliminary calibration. . . . .</i>	65
5.6	<i>Graphite target. NaI <math>\gamma</math>-spectrum with no conditions applied. . .</i>	66
5.7	<i><math>^{12}\text{C}</math> missing energy spectra. Target thickness <math>235\text{ mg}\cdot\text{cm}^{-2}</math> . . .</i>	66
5.8	<i>Cuts on missing energy spectra. . . . .</i>	67
5.9	<i>Graphite target. NaI <math>\gamma</math>-spectrum after application of conditions.</i>	68
5.10	<i>Water target. NaI <math>\gamma</math>-spectrum after selection of proton events. .</i>	68
5.11	<i><math>^{16}\text{O}</math> missing energy spectra. . . . .</i>	69

# List of Tables

2.1	Parameters of different scintillation materials . . . . .	11
2.2	Characteristics of the LeCroy HQV820 preamplifier. . . . .	17
4.1	Light collection efficiency for different crystal and diode sizes . .	43

# Chapter 1

## Introduction - The $^{12}\text{C}(\gamma, \text{p}\gamma')^{11}\text{B}$ Experiment

Photons, the force carriers of the electromagnetic interaction, can couple to the various nuclear currents, yielding information on nuclear structure and allowing the nucleus to be probed by photoabsorption. As a nuclear probe the photon has the advantage that its interaction is described by the well-known theory of Quantum Electrodynamics (QED). Since the electromagnetic interaction between the photon and the nucleon is weak (in comparison with the strong interaction between nucleons) the photon can probe the entire nuclear volume with only mild perturbation of the system. The relative weakness of the electromagnetic interaction ensures that the photon is unlikely to suffer initial state interaction (ISI) and permits first order perturbation theory to be used. The well-known description of nucleons as bags containing quarks with an impenetrable boundary [He94], although capable of explaining static nucleon properties, fails to account for the nucleon-nucleon short range correlations (SRC). An interaction between nucleons needs the exchange of a particle, the field quantum responsible for the interaction, which is able to traverse the bag's boundary. This led to the assumption that nucleons are surrounded by a mesonic cloud consisting of  $\pi, \rho, \omega$ , etc.. The interaction between nucleons in this picture is the continuous emission and absorption of virtual mesons by the nucleons. The interaction of an energetic photon with a nucleus is the interaction of the electromagnetic field with various currents induced by the constituents of the nucleus. The scale of phenomena probed depends on the wavelength  $\lambda = \frac{hc}{E_\gamma}$  of the photon, so that increasing the photon energy  $E_\gamma$  results in smaller wavelength  $\lambda$  and hence in better spatial resolution.

For  $E_\gamma < 1$  GeV the energy dependence of the photon absorption cross section can be divided into three regions (see Figure 1.1).

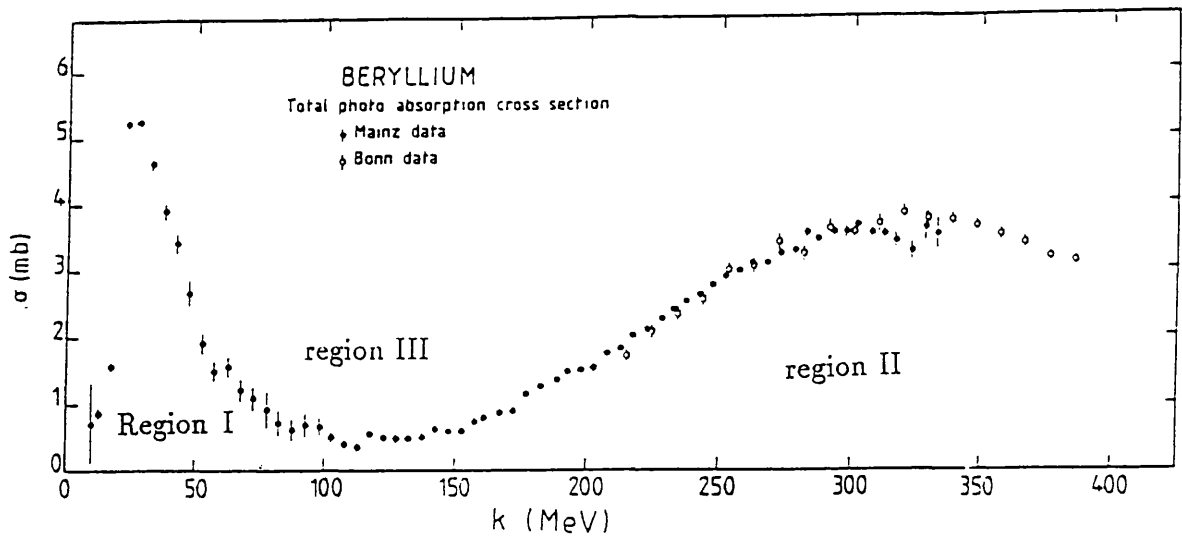


Figure 1.1: *Total photon absorption cross section in  $^9\text{Be}$*   
[Ar81]

The following will give a brief discussion of the three regions:

Region I in the energy range of a few tens of MeV is dominated by the Giant Resonances, mainly the Giant Dipole Resonance (GDR). These resonances are collective excitations of the nucleus and can be qualitatively understood using a hydrodynamic model of the nucleus.

The GDR is only one of the possible oscillations. In the hydrodynamic picture one classifies the oscillations into monopole, dipole or higher excitations. Each category is subdivided by distinct values of  $\Delta T$  and  $\Delta S$ .

Modes where the isospin remains constant ( $\Delta T=0$ ) are labeled isoscalar. If, in contrast, protons and neutrons change places in every element of volume then the z-component of the isospin changes from  $+\frac{1}{2}$  to  $-\frac{1}{2}$ , hence  $\Delta T=1$ . Such modes are called isovector. In addition the z-component of the spin can change

(spinflip with  $\Delta S=1$ ).

The most complicated case is where  $\Delta S=\Delta T=1$ , which -by analogy to beta-decay- are called "Gamow-Teller-Resonances".

It has to be realized that hydrodynamic models are only able to give a crude description of the Giant resonances. A microscopic description has to proceed from wave functions of the nucleons. In the presence of exchange terms or momentum dependent terms in the potential the formula for the total integrated electric dipole cross section is [Sh74]

$$\int \sigma(E)dE \approx 60 \frac{NZ}{A} (1 + \kappa) \text{ MeVmb}$$

Here the so-called enhancement factor  $\kappa$  is a measure of the exchange and momentum dependent parts of the nuclear force. N, Z and A denote the neutron number, the atomic number and the mass number, respectively.

The broad peak at  $\sim 300$  MeV in the total photon absorption cross section (region II) is due to the excitation of the  $\Delta(1232)$  resonance. The  $\Delta$ -isobar at 1232 MeV is the first excitation of the nucleon. It can be understood in terms of a spin-isospin flip of a quark with no change in orbital motion (Gamow-Teller excitation). This results in an unstable state which de-excites back to the ground state within a time of  $\sim 10^{-23}\text{s}$  - a typical time scale for the strong interaction - thereby emitting a  $\pi$ -meson. Thus the  $\Delta$ -state can be interpreted as a resonant state of the  $(N, \pi)$  system and its study in the nuclear medium is closely related to the in-medium behavior of the pion, the carrier of the strong force. The aim of experiments in this energy region is to gain information about the coexistence of the nucleon, the pion and the  $\Delta$ -isobar in the nucleus [Ga93]. This is an important configuration, because it modifies nuclear forces inside the nucleus and might provide the beginnings of an understanding of three-body

forces [He94].

The energy region intermediate between the nuclear collective resonances and nucleon resonances (region III) is often referred to as the quasi-deuteron region. Using phenomenological models, the reaction mechanisms taken into account in this region are the absorption of a photon by a single nucleon and the absorption of a photon by a correlated neutron-proton pair, coupled to form an  $S=1, T=0$  quasi deuteron (QD). Assuming that the photon is absorbed by a single nucleon leading directly to its ejection and leaving the residual nucleus relatively unperturbed (quasifree knockout, QFK) one is confronted with the problem of momentum mismatch between the photon and the ejected nucleon. Since the momentum mismatch must be balanced by the momentum of the nucleon in the nucleus before interaction the strength of QFK decreases with increasing energy. In the model where a photon is absorbed by a correlated nucleon pair the momentum mismatch can be balanced by relative initial momentum of the nucleon pair. Absorption of transverse photons is therefore more readily described by the QD model. The  $(\gamma, pn)$  reaction is generally dominant in this energy region but further experimental evidence for the QD picture lies in the similarity of the  $(\gamma, p_0)$  and the  $(\gamma, n_0)$  cross section, these reactions taking place when one nucleon is reabsorbed. QFK gives a much larger cross section for  $(\gamma, p_0)$  than for the corresponding  $(\gamma, n_0)$  cross section. This is because neutrons have no electric charge and hence the photon can couple only weakly to the magnetic moment (spin). However, it should be mentioned that final state interactions (FSI) can increase the  $(\gamma, n)$  cross section without the need to introduce two-nucleon interactions in the photoabsorption mechanism.

In QFK the residual nucleus is left in a  $1h$  (one hole) state relative to the target

nucleus unless inelastic scattering inside the target nucleus occurs. The simplest case in the QD model is where the two struck nucleons (most commonly a proton and a neutron, because only this combination possesses a dipole moment) are emitted leaving the residual nucleus in a 2h-state relative to the target nucleus. Another possibility is that only one nucleon is emitted, while the other correlated one has not enough energy to separate from the nucleus and returns to its initial state or makes a transition to an excited state. The latter process results in a residual nucleus which is left in a 1p-2h state. Taking processes into account where the residual nucleus is left in a 1h state or a 1p-2h state is frequently referred to as the modified quasi-deuteron (MQD) reaction mechanism. The fact that QD model approaches are more successful in describing the experimental results indicates that two body currents such as meson exchange currents (MEC) are important. Consequently, in order to gain a deeper insight into the photoabsorption mechanism, microscopic models rather than phenomenological models are necessary. Examples of such models are the Gari and Hebach model [Ga81] and the Random-Phase Approximation (RPA) models [Ca84] [Ry88]. However, none of those proposed to date have been completely free from criticism.

Due to the small cross section in the QD region (Region III, Figure 1.1) it is a non-trivial task to investigate this intermediate energy zone experimentally and it is only recently, with the development of high duty cycle electron accelerators and photon tagging facilities (see Chapter 5), that  $(\gamma, N)$  measurements with adequate energy resolution to separate distinct excited states in the residual nucleus have been feasible. Of course, the development of particle detectors with good energy resolution ( $\leq 0.5$  MeV for the light nuclei under investigation) has also been important in this respect. To account for the small cross sections,

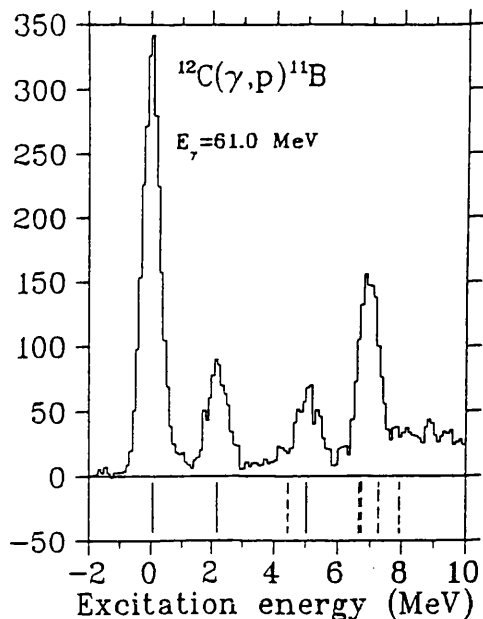


Figure 1.2: *Excited states in  $^{11}\text{B}$*   
[Ni90]

the detectors used in photonuclear experiments should cover large solid angles in order to enable the execution of experiments in finite time.

A relatively complete set of data has been gathered for the  $^{12}\text{C}(\gamma, p)^{11}\text{B}$  reaction at photon energies around 60 MeV. The corresponding excitation energy spectra (Figure 1.2) exhibit four main peaks stemming from the population of the  $^{11}\text{B}$  ground state ( $\frac{3}{2}^-$ ), the excited states at 2.12 MeV ( $\frac{1}{2}^-$ ) and 5.02 MeV ( $\frac{3}{2}^-$ ) and from a strong excitation at  $\sim 7$  MeV of an unresolved triplet of states ( $\frac{7}{2}^-$ ,  $\frac{1}{2}^+$ ,  $\frac{5}{2}^+$ ). The relative strength of the states at  $\sim 7$  MeV, which have large two hole, one particle (2h,1p) structural components is most striking, because it is far in excess of that measured in  $^{12}\text{C}(e, e'p)^{11}\text{B}$  which mainly probes single hole (1h) strength. However, the question of interpretation of this phenomenon is still left open and conclusions remain clouded, because up until now, the achieved experimental resolution was not sufficient to clearly resolve the  $\frac{7}{2}^-$

(6.74 MeV), the  $\frac{1}{2}^+$  (6.79 MeV) and the  $\frac{5}{2}^+$  (7.29 MeV) states. As a matter of fact, any contemporary experiment relying solely on proton detection will fail to separate the states at 6.74 and 6.79 MeV. Therefore, in the  $^{12}\text{C}(\gamma, p\gamma')^{11}\text{B}$  experiment the resolution of the relative population of the triplet of states at  $\sim 7$  MeV is - as the reaction formula indicates - intended to be performed via the immediate  $\gamma$ -ray decay of the excited residual states of  $^{11}\text{B}$ . The rejection of any de-excitation  $\gamma$ -rays which originate from cascades from higher populated residual states requires efficient proton detectors with reasonable energy resolution which serve as triggers for the data acquisition.

The remainder of this thesis is concerned with the description (Chapter 2), the optimization (Chapter 3), the numerical simulation of the detection characteristics (Chapter 4) and the test (Chapter 5) of one of the proton detectors used in the  $^{12}\text{C}(\gamma, p\gamma')^{11}\text{B}$  experiment.

## **Chapter 2**

# **The Proton Detector**

Table 2.1: Parameters of different scintillation materials

Parameter	BaF <sub>2</sub>	BGO	CsI(Tl)	NaI(Tl)
Density(g/cm <sup>3</sup> )	4.88	7.13	4.5	3.7
Radiation length(cm)	2.03	1.13	1.86	2.6
$\langle \lambda_{scint} \rangle$ (nm)	325, 225	480	550	410
Decay constant (ns)	620, < 1	300, 60	~900	230
Photons/MeV at 20°C	8500	0.5-1×10 <sup>4</sup>	4.5×10 <sup>4</sup>	4×10 <sup>4</sup>
Afterglow (% after 3ms)	-	0.05	< 5	< 5
Hygroscopicity	-	-	(-)	yes
Mechan.,therm. stability	(good cleavage)	good	very good	(fair cleavage)
Radiation resistance	very good	medium	fair	fair

In order to examine charged particles at medium energy (energy range of several tens of MeV), it is necessary to develop a detector with high stopping power and good energy resolution. Because of the small cross section (1-10 $\mu$ b/sr) for photon absorption in the QD region and the relatively low intensity of tagged photons ( $\sim 10^6 s^{-1} MeV^{-1}$ ), such a detector should also have a large solid angle.

## 2.1 Scintillation Material

Solid-state, high-purity germanium detectors are in common use in medium energy light-particle spectrometers but are expensive. Much cheaper scintillators with high density and good light output could meet the above requirements. Table 2.1 shows the main parameters of some well-known materials. The tabulated numbers are taken from Ref. [Gr88].

Compared to other inorganic scintillation materials, thallium doped cesium iodide (CsI(Tl)) has the best light yield, which is important for good energy

resolution. The fact that CsI(Tl) is a material of reasonably high density allows the stopping of charged particles with crystals of moderate thickness. Furthermore, CsI(Tl) is cheap and has superior handling qualities to thallium doped sodium iodide (NaI(Tl)), the most common material in the past, due to its spectral matching to bialkali photomultipliers (PMs). CsI is a soft, non-brittle material which can be easily machined or cut and is only slightly hygroscopic. The properties of this material have been known for many years, but nevertheless it was rarely used. This was partly due to its long decay time and the low quantum efficiency ( $\sim 10\%$ ) when used in conjunction with a bialkali photomultiplier. Many tables suggest that CsI(Tl) gives a lower light yield than NaI(Tl), because the lower quantum efficiency of PMs for its scintillation light is not taken into account. It should also be mentioned that the light output depends on the Tl concentration. However, with the availability of large-area silicon photodiodes, whose spectral peak sensitivity is well matched to the scintillation emission maximum at 550 nm producing 70% quantum efficiency, CsI(Tl) has become a highly effective material for low cost medium-energy charged particle spectroscopy, especially in situations where counting rates are not too high. When using a PIN diode as the readout system the long decay time of CsI(Tl) becomes relatively unimportant, because for large area diodes an integration time of at least  $\sim 3\mu\text{s}$  (ideally  $\sim 6\mu\text{s}$ ) should be used in the subsequent signal shaping and amplification circuitry to obtain a reasonably good signal-to-noise ratio. It should also be mentioned that unlike photomultipliers, which often show hard-to-predict excursions in gain, PIN-diodes are inherently stable devices, an important aspect for a reliable detection system.

## 2.2 Mechanical Construction

The heart of the proton detector is an array of twenty  $25 \times 25 \times 30 \text{ mm}^3$  CsI(Tl) crystals, arranged in form of a  $4 \times 5$  matrix. Using the Bethe-Bloch-formula (see appendix A), the thickness chosen (30 mm) was found to be sufficient to stop 90 MeV protons. Fine abrasives were employed to give the crystal surfaces a matt finish, except the diode-coupled surface, which was polished with liquid detergent, following the manufacturer's recommendation. Before wrapping, all surfaces were cleaned with high purity alcohol.

Stretched layers of PTFE (PolyTetraFluoroEthylene,  $\text{C}_2\text{F}_4$ ) tape, which allowed coverage of the surfaces in an uniform way, were chosen to serve as a diffusive reflective wrapping with minimum transmission. Each crystal is wrapped in  $\sim 300 \mu\text{m}$  thick PTFE to give an optimum in light collection efficiency. Thus, the scintillator blocks are separated from each other by a total of  $\sim 600 \mu\text{m}$  thick PTFE foil. Optical coupling of the diodes to the crystals is by transparent silicone elastomer.

For mechanical protection and stability the array is contained in an aluminium box which has a  $12.5 \mu\text{m}$  aluminium foil window to ensure electrical shielding and light tightness. The thickness of the window has to be thin to keep straggling of the protons to a minimum. In the present case, the straggling of the protons in aluminium is smaller than in PTFE.

All diodes are cooled to limit the thermal generation of charge carriers in the depletion layers of the diodes. The cooling system consists of three Peltier junctions connected in series to produce a power input of 15 W, which is enough to reduce the temperature by 15 K, although this value is somewhat dependent on the ambient temperatures. The thermal coupling to the ceramic substrates of

the diodes is by a brass plate and heat transfer paste at all important junctions. To monitor the performance of the cooling system, a small solid-state temperature sensor was embedded in the brass cooling plate. Feedback from this sensor can be used to control the Peltier current and hence stabilize the temperature.

In order to select charged particles produced in the experimental target, two thin  $\Delta E$  NE102 plastic scintillators, positioned as in Figure 2.2, combine with the CsI array to form a  $\Delta E$ - $\Delta E$ -E telescope .

The element near to the target has dimensions  $70 \times 60 \times 0.5 \text{mm}^3$  and its edge is coupled via a lucite light guide to a 50mm, type EMI 9954 photomultiplier (PM) tube. The second element, placed directly in front of the CsI(Tl) array, has dimensions  $110 \times 85 \times 1 \text{mm}^3$  and is read out by two PM tubes of the same type. Its dimensions are chosen smaller than the CsI array to exclude those edge events where an energetic proton might not stop in the outer CsI(Tl) blocks. The front and rear scintillator sheets are placed 50mm and 140mm from the target respectively.

Figure 2.1 shows a scatter-plot obtained in a test run at the accelerator facility in Lund (Sweden); the x-axis on this plot gives the pulse height in one of the E detectors and the pulse height in the rear  $\Delta E$  detector constitutes y-axis. Since the energy loss of protons in the  $\Delta E$  detectors is higher than for electrons it is possible to identify and select proton events.

Finally, the whole telescope is fixed to an aluminium housing which pivots around the target, allowing measurements at different angular positions to be made.

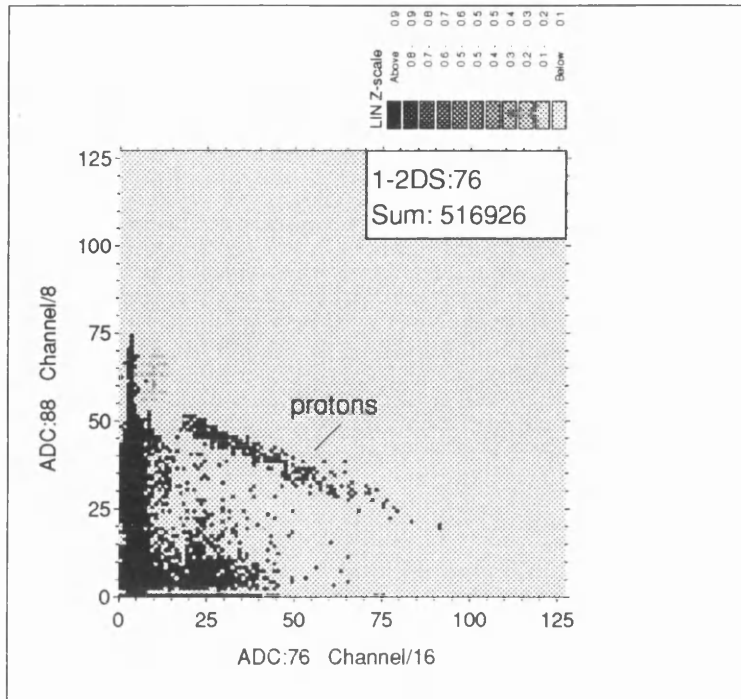


Figure 2.1:  $\Delta E, E$  scatter-plot obtained in the  $^{12}\text{C}(\gamma, p\gamma')^{11}\text{B}$  test run in Lund

## 2.3 Electronics for the CsI(Tl) Scintillation Readout

Hamamatsu type S2744 ( $10 \times 20 \text{mm}^2$  active area) silicon PIN-diodes are used to collect the CsI(Tl) scintillation light. The reason for using PIN-diodes lies in the high quantum efficiency at  $\sim 550 \text{nm}$  when compared with alkali PMs. Another promising possibility would be the use of silicon avalanche photodiodes which provide internal charge multiplication by typical factors of a few hundred resulting in excellent signal to noise ratio. However, the use of these diodes does not yet improve upon results obtained with conventional silicon PIN diodes [Ko93].

Since the signals obtained from photodiodes are small, low noise electronics is extremely important for the subsequent signal processing. The first stage in

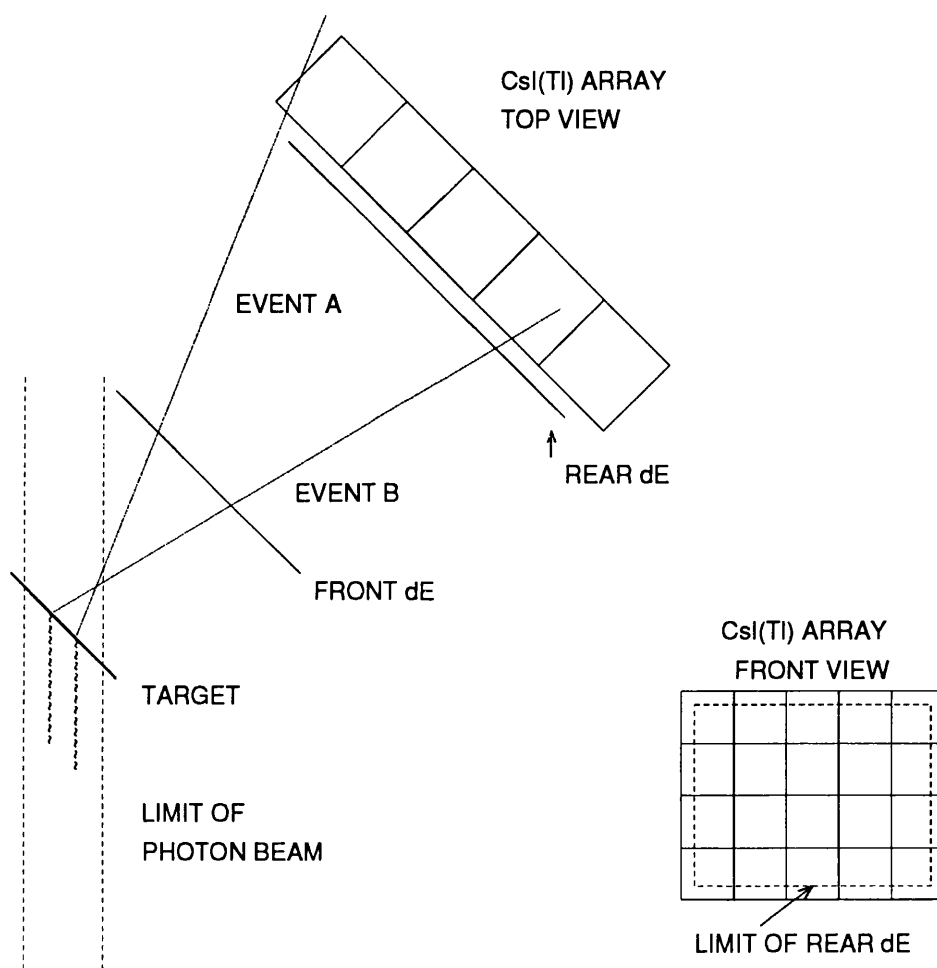


Figure 2.2: Schematic diagram of the  $\Delta E, E$  telescope in a typical experimental geometry

Table 2.2: Characteristics of the LeCroy HQV820 preamplifier. The input capacitance is the terminal capacitance of the photodiode ( $\sim 150\text{pF}$  at 20 V reverse voltage for the diode used in the present application)

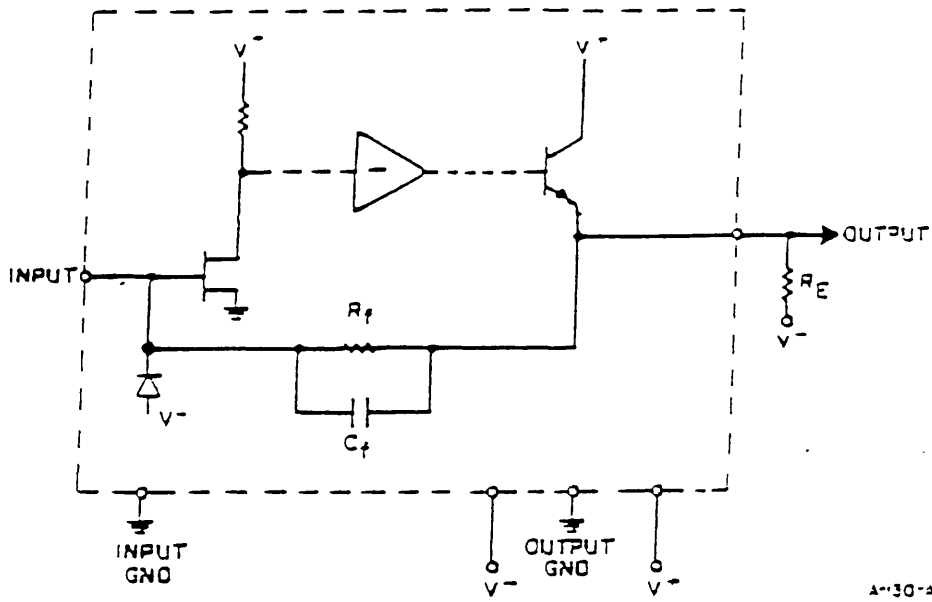
Noise Minimum (R.M.S. Electrons)	250 (Input capacitance 10pF)
Noise slope	$6 e^- / \text{pF}$ (Shaping time $3\mu\text{s}$ )
Signal Risetime	10 ns + 0.4ns per pF of input capacitance
Signal Decay Time Constant( $\mu\text{s}$ )	$200 \pm 20\%$
Feedback Resistor ( $M\Omega$ )	100

signal processing is preamplification using a charge sensitive preamplifier. The advantage of this type of preamplifier lies in its insensitivity to changes in capacitance of the photodiode, which occur with variations in temperature. In our case, compact, low noise charge sensitive hybrid FET preamplifiers (LeCroy HQV820 photodiode preamplifiers [LC92]) were coupled to the diodes. Table 2.2 shows some characteristics of this type of preamplifier. The numbers are taken from Ref. [LC92].

Figure 2.3 shows a simplified circuit diagram of the LeCroy HQV820 preamplifier.

In this circuit the output voltage is obtained by integrating the charge  $Q$  of the incoming pulse on the capacitor  $C_f$ . It can be shown [Kn79] that the output voltage  $V_{out}$  is approximately given by

$$V_{out} \approx \frac{Q}{C_f}$$



A-30-A

Figure 2.3: *Input and output circuit of one channel of the HQV800 series*

The purpose-built shaping amplifiers shown in figure 2.4 complete the amplification system.

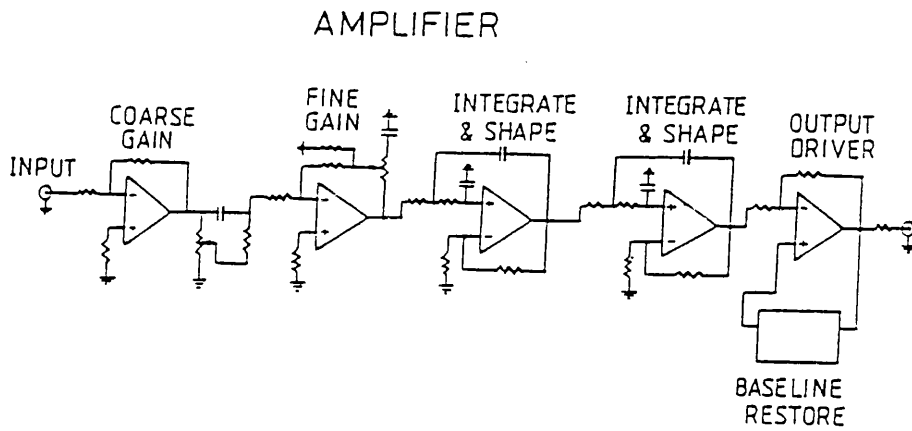


Figure 2.4: A simplified diagram of the shaping amplifier

# **Chapter 3**

## **Measurements**

### 3.1 Optimization of the Setup

Optimum energy resolution implies optimum signal to noise ratio.

The noise, when expressed in terms of the equivalent noise charge (*enc*), can be approximated as follows [De69].

$$(\text{enc})^2 \approx \epsilon^2 \left( \frac{kT}{2R_g} \tau + \frac{eI_g}{4} \tau + \frac{kTC^2}{2g_m \tau} \right) \quad (\text{eqn. 1.})$$

where

<b>T</b>	≡	temperature of the FET
<b>k</b>	≡	Boltzmann constant
<b>R<sub>g</sub></b>	≡	resistance of the parallel combination of the diode load and feedback loop resistors
<b>τ</b>	≡	shaping amplifier RC time constant
<b>e</b>	≡	electron charge magnitude
<b>I<sub>g</sub></b>	≡	diode leakage current (dark current)
<b>g<sub>m</sub></b>	≡	FET transconductance (≈50 mAV <sup>-1</sup> )
<b>C</b>	≡	sum of the diode and FET capacitance
<b>ε</b>	≡	shaping parameter (ε = e <sup>1</sup> ≈ 2.7 ∼ Gaussian shaping)

If SI units are input to this equation, the *enc* is obtained in Coulombs.

To achieve the optimum setup of the combination diode, preamplifier and amplifier, measurements have been made varying the shaping time and the reverse voltage applied to the diode.

Standard commercial nuclear spectroscopy electronics consisting mainly of a low noise charge sensitive preamplifier, a main amplifier with coarse adjustable shaping time and an Analogue to Digital Converter (ADC) operated in peak sensing mode have been used. The setup is shown in Figure 3.1.

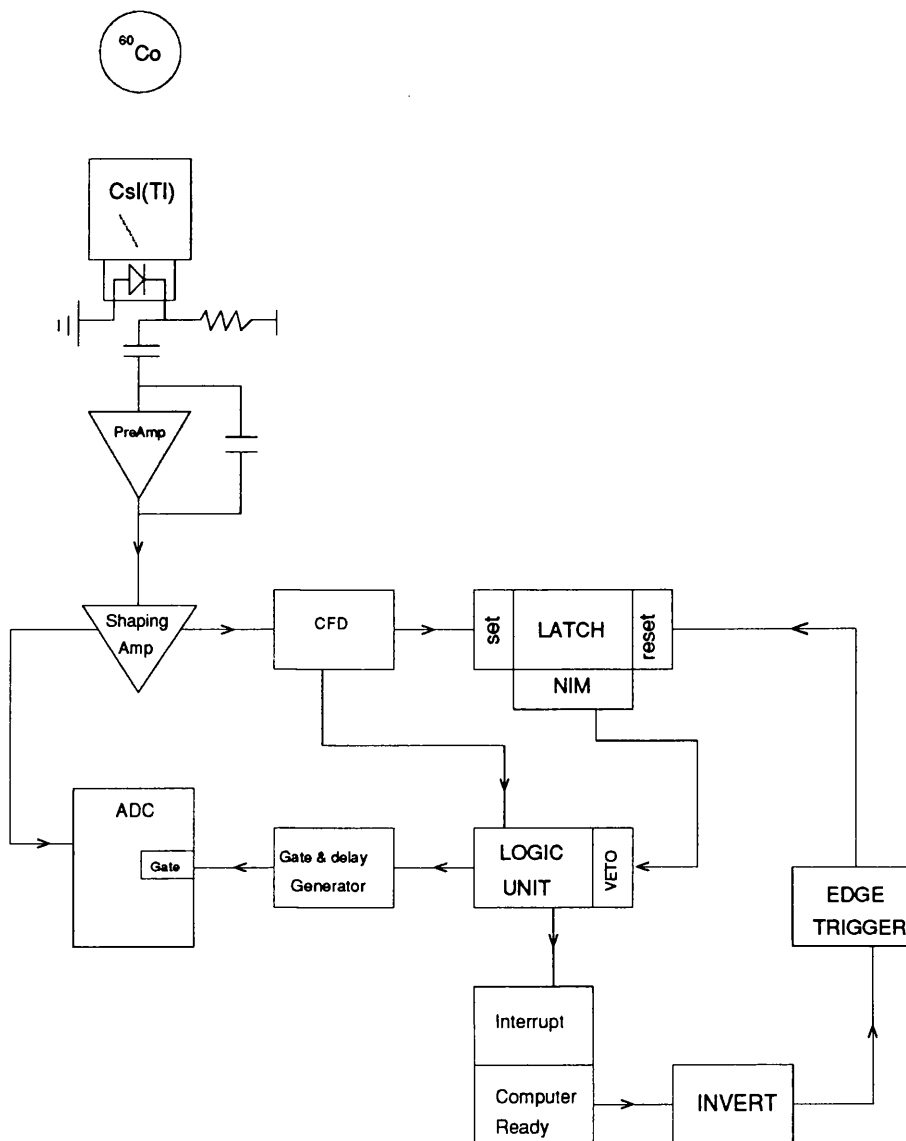


Figure 3.1: Test experimental setup

The following will give a short explanation of the setup.

After passing the preamplifier and the amplifier one (delayed) branch of the signal is fed into a CAMAC peak-sensing ADC which interfaces with a VME computer. In order to trigger a gate for the pulse the second branch is fed into a CFD (Constant Fraction Discriminator). One of the CFD outputs is the input for a logic unit, the other one starts a dual gate and delay generator (used in the latch mode) whose stop comes from the VME computer. During the time between a start and a stop the processing of the input of the logic unit is vetoed, i.e. only signals which arrive after the computer is ready are accepted for processing. These signals give a gate to the ADC and an interrupt, which triggers data readout from the ADC. An adjustable delay allows a coincidence to be made between the logic gate pulse and the peak output from the amplifier. The data was read out by the computer using the ACQU data acquisition system [An93], and transferred to an ALPHA workstation for display. One could, in principle, replace the whole apparatus following the shaping amplifier by a commercially available multi-channel analyzer (MCA). However the advantage of the setup used is that it can be easily extended for larger scale tests. In particular it is possible to read multiple ADCs and easily change the trigger logic.

Variations in the reverse voltage have an effect on both the capacitance and the leakage current of the diode. To obtain best results the values of these two quantities should be small (this is immediately evident by looking at equation 1.). Typical curves for the variation of the capacitance and leakage current with reverse voltage are shown in Figure 3.2. The diagrams are taken from [Ha94]

Figure 1: Spectral Response

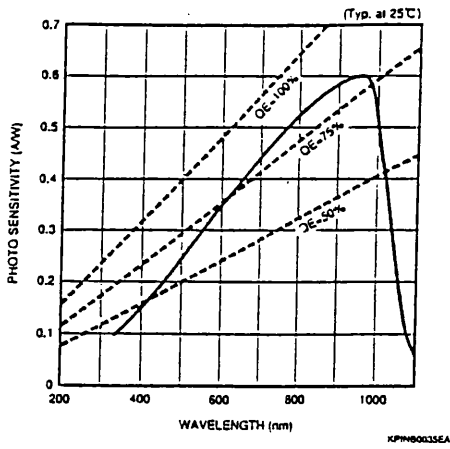


Figure 2: Terminal Capacitance vs. Reverse Voltage

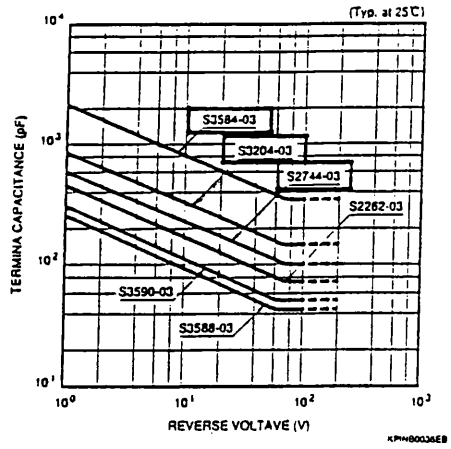


Figure 3: Dark Current vs. Reverse Voltage

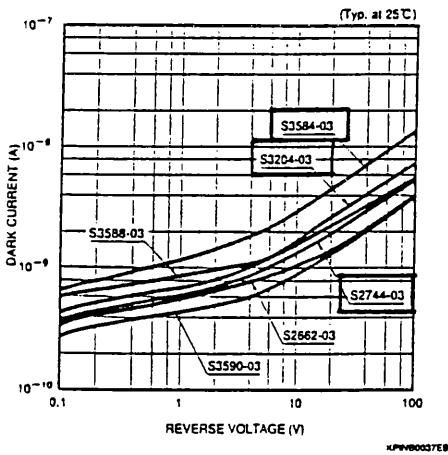


Figure 4: Dark Current vs. Temperature

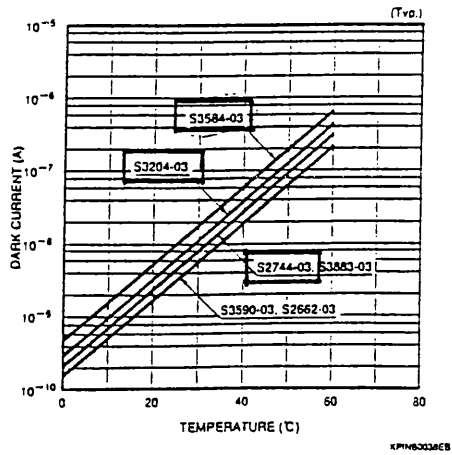


Figure 3.2: Capacitance and leakage current for the PIN-Diodes employed in the present work.

In Figure 1, the dashed lines show constant quantum efficiency. The diodes applicable to this work are indicated in Figures 2, 3 and 4.

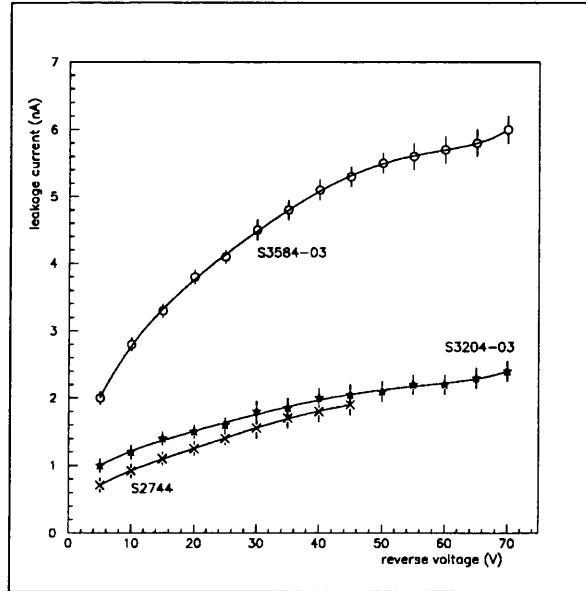


Figure 3.3: Measured leakage currents of the diodes at room temperature in light-tight boxes

To get an impression of the validity of these curves the leakage current of the  $10 \times 20 \text{mm}^2$  (Hamamatsu S2744),  $18 \times 18 \text{mm}^2$  (Hamamatsu S3204-03) and  $28 \times 28 \text{mm}^2$  (Hamamatsu S3584-03) PIN-diodes were measured using a picoammeter. The results are shown in Figure 3.3.

Compared to the values given in the technical data sheet the measured dark current is up to 50% lower for the S2744 and S3584-03 diodes and up to 80% lower for the S3204-03 diode. Knowing the leakage current of the diodes and taking the capacitance from Figure 3.2 the noise for different reverse voltages can be evaluated from equation 1. (Figure 3.4).

The full width at half maximum (fwhm) of the photoelectric peaks produced by

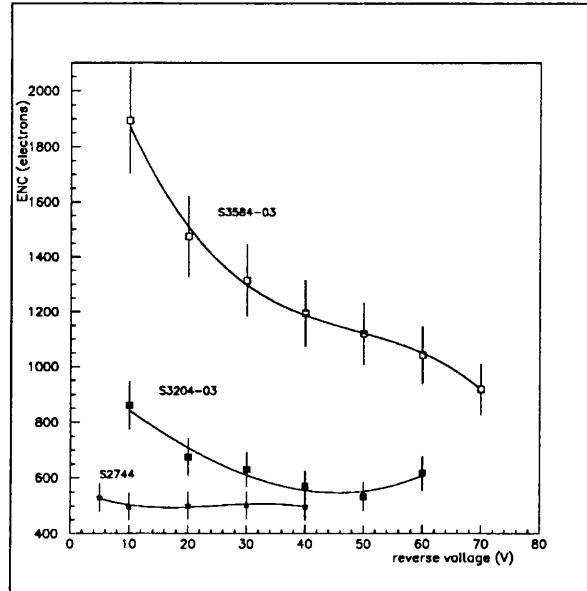


Figure 3.4: Reverse voltage dependence of the noise. Shaping time  $3\mu\text{s}$ . The error bars are due to the measurement of the leakage current.

a  $^{60}\text{Co}$  source provides a measure of the resolution of the detector. The energy equivalence of the electronic noise can be expressed as follows

$$fwhm_{1\text{MeV}} = \frac{enc}{\eta\xi\tau} \cdot 2.355 \text{ MeV} \quad (\text{eqn. 2.})$$

where

$enc$  is the electronic noise charge expressed in electrons rms (calculated),  
 $\eta$  denotes the quantum efficiency ( $\sim 70\%$ ),  
 $\tau$  stands for the photon yield per MeV ( $\sim 4.5 \times 10^4$ ), and  
 $\xi$  is the light collection efficiency (see chapter 4.1.2).

Thus, for a given combination of wrapped crystal and diode, the fwhm is directly proportional to the noise and consequently this proportionality should be observed in a measurement. The simple setup of Figure 3.1 was used to check this dependence.

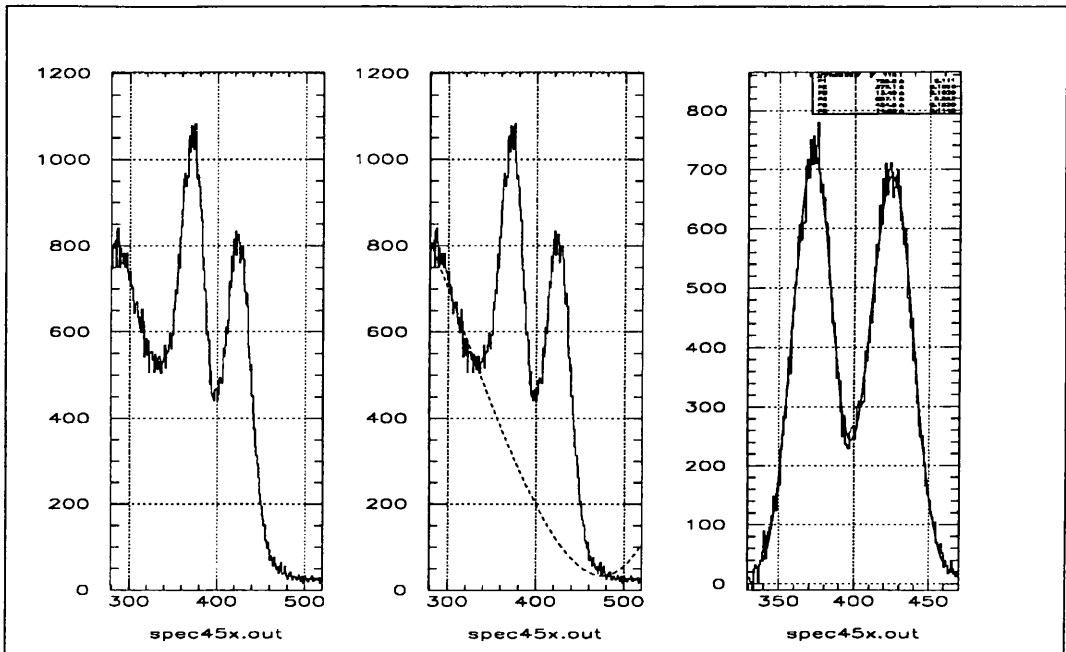


Figure 3.5: *Fitting and Subtracting the background.*

Depicted are the 1.17 and the 1.33 MeV peaks produced by a  $^{60}\text{Co}$  source. The leftmost picture shows the raw spectrum. The dotted line in the central picture shows the fitted background. The rightmost picture shows the background subtracted spectrum.

To analyse the obtained spectra, a Macro (command procedure) was written in PAW (Physics Analysis Workstation; a utility for analyzing and displaying experimental data on a computer graphics display) to make a non-linear least squares fit to the experimental spectra taken with a  $^{60}\text{Co}$  source, in order to take the Compton-background into account and to make a double Gaussian fit to the spectra after background subtraction. The background was approximated with a third order polynomial. This procedure was applied to all spectra. Only relative values for the resolution are important to this investigation. The steps in this procedure are shown in Figure 3.5.

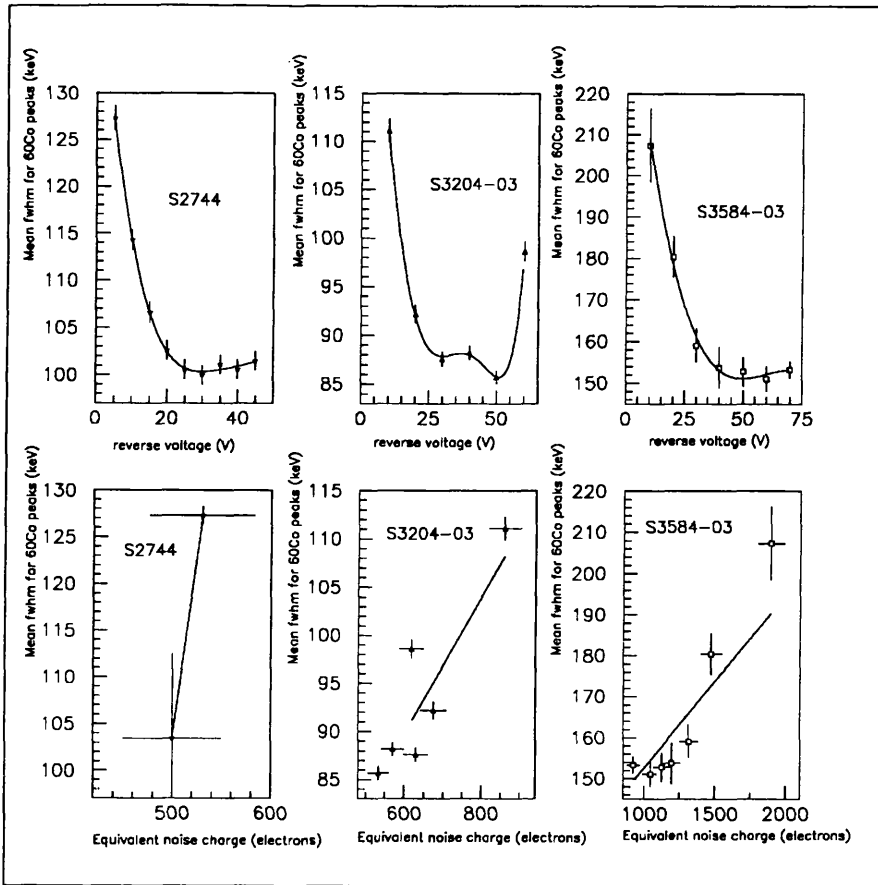


Figure 3.6: Resolution for different reverse voltages

The results of this measurement are shown in Figure 3.6 where the mean of the fwhm of both  $^{60}\text{Co}$  peaks is plotted against the reverse voltage and the calculated noise. In the case of the smaller diodes (S2744 and S3204-03) a  $2.5 \times 2.5 \times 3 \text{ cm}^3$  crystal was used, in case of the S3584-03 diode, whose dimensions are  $2.8 \times 2.8 \text{ cm}^2$ , a  $5 \times 5 \times 5 \text{ cm}^3$  crystal was used.

It can be seen from the  $\frac{fwhm}{enc}$  diagrams that eqn. 1 gives only an estimation for the noise. Eqn. 1 only takes account of the 'white' noise; i.e. thermal and shot

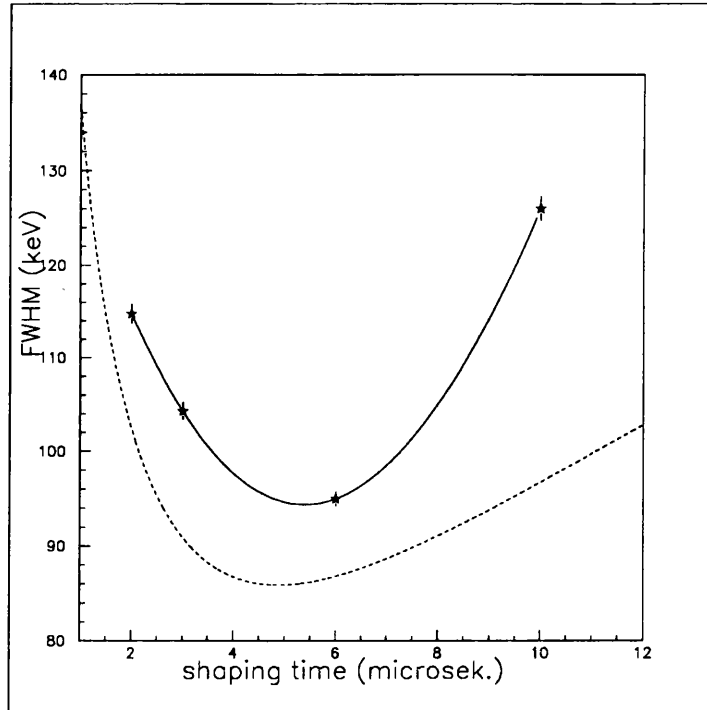


Figure 3.7: *Shaping time dependence of the noise.*

The experimental data points were fitted with a 3rd order polynomial. The dotted line gives the shaping time dependence of the enc as in eqn. 1 (arbitrarily scaled).

noise; not included is the flicker or modulation noise in the FET channel, with a frequency dependence varying approximately as  $\frac{1}{f}$ .

In addition it should be remembered that the capacitances of the diodes have been taken from a data sheet ([Ha94]) which gives only typical values.

The effect of varying the shaping time for the S2744 diode is shown in Fig. 3.7. By far the best result is obtained with  $6\mu\text{s}$  shaping time; however in most experiments  $3\mu\text{s}$  shaping time is preferred for counting rate reasons.

The experimentally obtained minimum is consistent with the value found, when

looking at eqn. 1 as a function of  $\tau$  and searching for the minimum.

### **3.2 Effects of varying the reflective wrapping on the light collection efficiency and the signal-to-noise ratio.**

Light collection efficiency (LCE) depends on the reflective wrapping. Several materials have been tested for the wrapping including filter paper, aluminium foil and PTFE tape.

Since the LCE and the signal-to-noise ratio were obviously rather poor for both filter paper and aluminium foil, no further attempts have been made to optimize wrappings containing these materials.

Several different PTFE tapes have been tested showing that stretched layers of 'Crosslite' PTFE are the best choice for the wrapping as, unlike the other tapes, this version allows an almost uniform coverage of all surfaces. The measured parameters of this wrapping are  $\sim 10 \text{ mg}\cdot\text{cm}^{-2}$  and  $\sim 70 \mu\text{m}$  thickness per layer. Compared to other tapes for approximately the same wrapping thickness a relative improvement in the light output of  $\sim 10\%$  was observed.

Using teflon tape as a diffusive reflector one has to be careful to avoid any pressure applied to the wrapped crystal, since this causes dark areas in the white teflon layers resulting in poorer resolution and slightly reduced light output. The dependence of the resolution and the light output on the number of teflon layers is shown in Figure 3.8.

It should be noticed in Figure 3.8 that the unexpected values of the above quantities for 7 teflon layers are a consequence of using too small an aluminium box

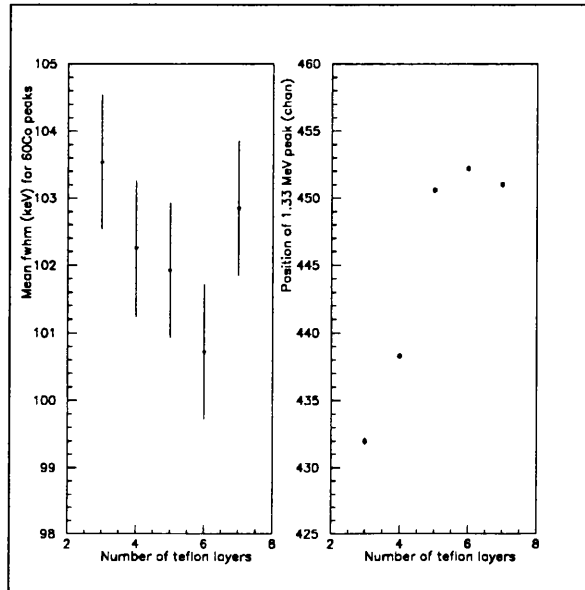


Figure 3.8: Resolution and light output vs. number of teflon layers

which compressed the teflon. An aluminium box is necessary for mechanical protection, electrical shielding and to prevent the external light increasing the leakage current of the diode and hence the noise.

Furthermore it can be seen that 5 layers of teflon tape provide a sufficiently good wrapping to obtain a high light output.

It is not totally correct to measure the wrapping performance in terms of the number of teflon *layers*, because the process of wrapping the crystal results in different effective wrapping thickness. However, the variations in wrapping thickness were found to be relatively small ( $< 8\%$ ).

The measurements with different numbers of teflon layers implied frequent re-assembling of the detector, which was sometimes done with non-optimum surface conditions. Ideally, the crystal surfaces have to be clinically clean. This

implies the use of gloves and antistatic tissues. After very careful preparation of the crystal surface excellent results have been obtained with only 4 layers of PTFE, which were attached to the crystal with great care.

### 3.3 Uniformity Measurements.

Considering that charged particles in real experiments can enter the detector at different positions and with different incident angles, thus producing scintillation quanta in different areas of the crystal, it is of great advantage for the experimentalist to have a uniform light collection.

A strong dependence of the light collection efficiency on the position of the generated photons is usually found only for relatively large scintillators where attenuation of scintillation light in the scintillating material plays an important rôle.

Nevertheless, when dealing with smaller crystals with a high reflectivity of wrapping read out by a (relative to the crystal dimensions) small-active-area diode, the multiple reflections of the scintillation photons result in a non-negligible flight-path which highlights the importance of an attenuation length and losses on reflection, thus the question of uniformity becomes a nontrivial one.

Therefore measurements have been carried out in order to investigate the difference in light output and resolution for different regions of generation of scintillation quanta. Figure 3.9 shows the setup used for this experiment.

When using the positron emitting  $^{22}\text{Na}$  source, which due to annihilation produces back-to-back 511 keV photons, this setup allows scanning of the crystal

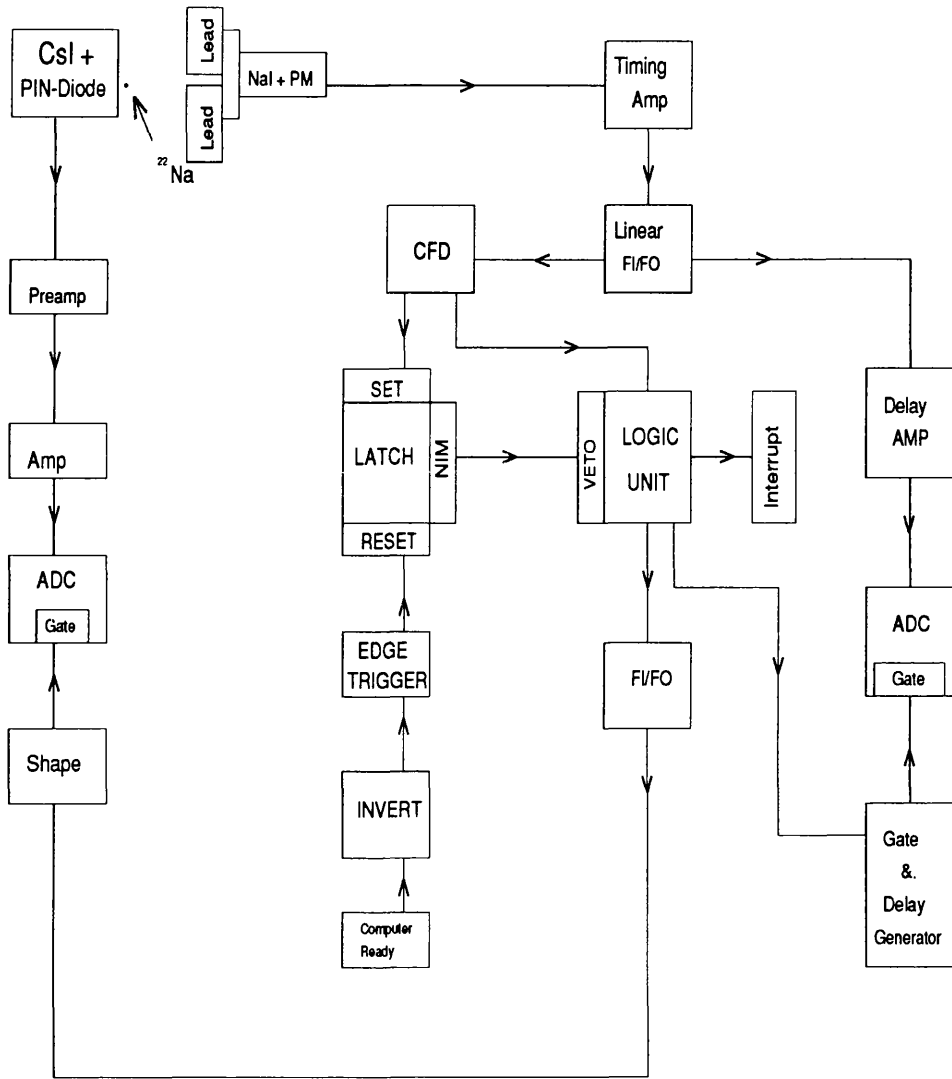


Figure 3.9: Setup for uniformity measurements

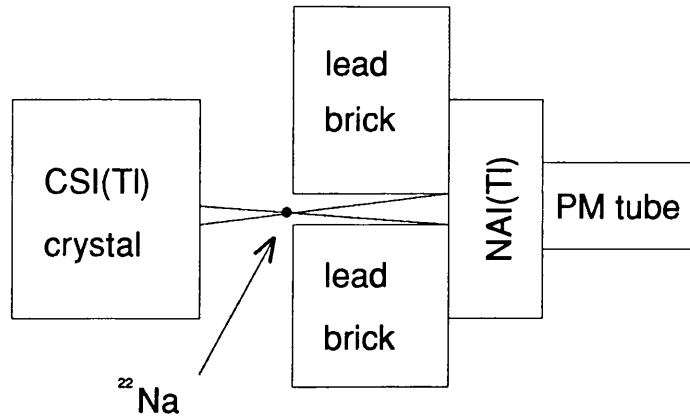


Figure 3.10: *Visualization of the Geometry*

with a collimated beam of  $\sim 0.3$  mm radius. Figure 3.10 shows that this value is determined by the size of the hole in the lead brick and the distances relative to the source. The basic function of the setup used is to obtain a pulse height spectrum of the CsI(Tl) detector for  $^{22}\text{Na}$  events, where a coincident pulse above a certain threshold in the NaI(Tl) detector is present; i.e. the NaI(Tl) detector gives the gate for such CsI(Tl) pulses thereby triggering data readout from the ADC on the left hand side in Figure 3.10. In order to enable the setting of the threshold just below the 511 keV photo-electric peak the pulse height spectrum of the NaI(Tl) detector is also recorded (ADC on the right hand side in Figure 3.10). To get an impression of the cleanness of the scan the percentage of random coincidences has been measured. This was done by setting the gate at uncorrelated signals. It was found that less than 5% of all coincidences were randoms.

Three different crystal sizes ( $25 \times 25 \times 30 \text{ mm}^3$ ,  $25 \times 25 \times 60 \text{ mm}^3$  and  $50 \times 50 \times 50 \text{ mm}^3$ ) read out by the three diodes mentioned before have been checked for uniformity. The smaller diodes were coupled to all crystals, the biggest only to the  $50 \times 50 \times 50 \text{ mm}^3$  crystal. All crystals were given a  $\sim 250 \mu\text{m}$  thick PTFE wrapping. The scan was performed by recording the pulse height spectrum obtained at several illuminated positions along the length and breadth of a CsI(Tl) crystal. Light output was given by the peak position of the 0.511 MeV photopeak and for this purpose all pulse height spectra were fitted with a Gaussian. The relative variations in light output found were less than 2% for the  $5 \times 5 \times 5 \text{ cm}^3$  and the  $2.5 \times 2.5 \times 6 \text{ cm}^3$  crystals and less than 1% for the  $2.5 \times 2.5 \times 3 \text{ cm}^3$  crystal.

The scan of the front surfaces of the crystals showed no measurable variation in light output, and contributions to the overall uniformities stemming from front face uniformities were negligible. However, for the two smaller sized crystals the scan of the side surface of the crystals revealed a noticeable dependence of the light output on the distance from the diode (see Figure 3.11).

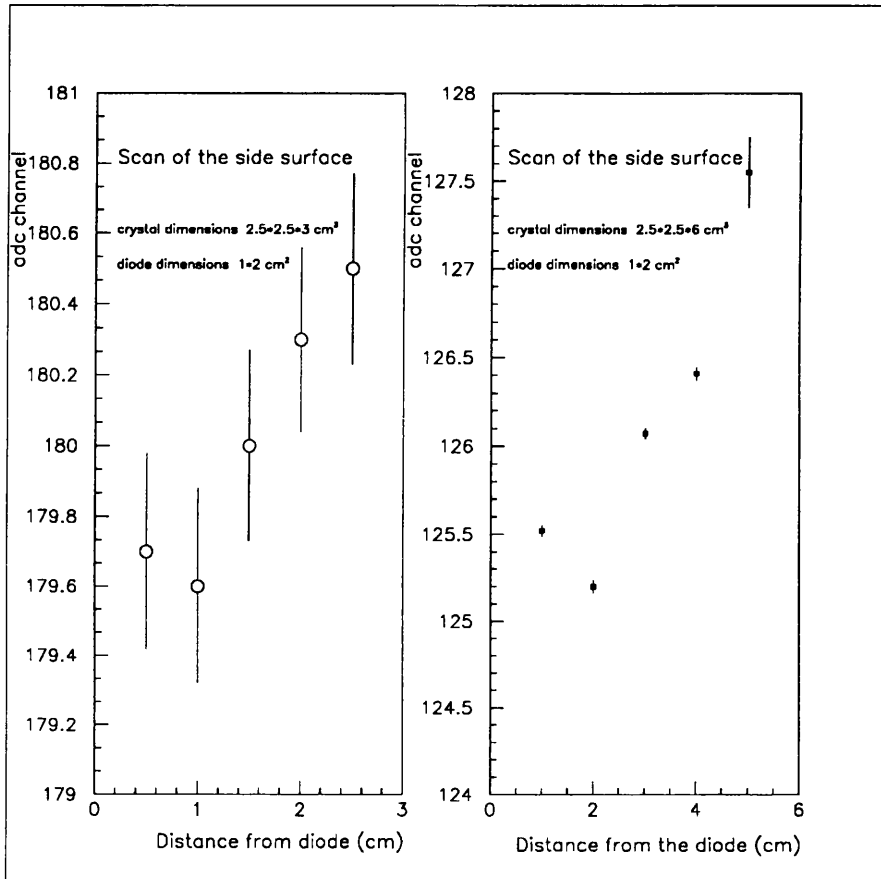


Figure 3.11: *Position dependence of the light output*

# **Chapter 4**

## **Monte Carlo Simulations**

## 4.1 Simulation of the Light Collection Efficiency

### 4.1.1 Description of the models

In order to gain more insight on how the light collection efficiency will vary for different crystal sizes, diode dimensions and wrapping reflectivities, two Monte Carlo models have been developed to model scintillation light transport within a CsI crystal.

The crystal under consideration is assumed to be of rectangular shape and separated from the reflector by an infinitesimal layer of air. Further assumptions are that the crystal surfaces are smooth (resulting in specular reflection) and the wrapping material is diffusely reflective. The smoothness of the crystal surfaces was assumed to keep the models relatively simple and easy to survey.<sup>1</sup> The first model is intended to simulate the light output in crystals with totally diffuse wrappings giving a uniform scattering angular distribution  $P(\theta)$  (perfect Lambert diffusers), whereas the second model was developed to study the transition from specular to diffuse reflection and is an attempt to simulate non-lambertian reflectors. Furthermore this model can easily be used to simulate specular reflection.

The only difference between the two models lies in the direction of a scintillation photon after reflection by the wrapping, which is completely arbitrary (uniform scattering probability) in the first model, while in the second it is correlated to a greater or lesser degree to the incident photon direction. A description of the

---

<sup>1</sup>It was experimentally checked, if this simplification is justified. Using the same wrapping thickness and the same crystal - once with smooth surfaces and once with rough surfaces - no measurable difference in light output was observed

second model follows.

The co-ordinates of production of the photon can be either directly input to the program from a parameter file or can be obtained by using a uniform random number generator. The initial direction  $i\vec{d}$  of the photon is assumed to be isotropically distributed.

After calculation of the first point of intersection with the crystal surface, an attenuation length determines whether or not the photon was absorbed inside the scintillation material (this is done by using an exponentially distributed random number). If not absorbed it is checked if the photon has entered the area of the crystal surface which is coupled to the diode, otherwise the incident angle is calculated and a comparison with the critical angle  $\theta_c = \arcsin \frac{1}{n}$  is made. If the incident angle  $\theta_i$  is smaller than  $\theta_c$  the photon will (*in this model*) encounter the reflector and there be transmitted with a probability  $1 - \text{reflectivity}$ ; otherwise it will undergo total internal reflection.

This handling of internal reflection is not totally correct but gives a reasonably good approximation. The correct way of describing internal reflection is to use the Fresnel equations, which do not only depend on the incident angle, but also on the polarization of the electromagnetic wave. Figure 4.1 shows the reflectance function for the transverse electric (TE) and the transverse magnetic (TM) modes when using the Fresnel equations. An arbitrary polarization direction represents some linear combination of these two special cases and would lie somewhere in between these curves. In the model described here, the reflectance function has been approximated with a step function which gives the value zero for  $\theta_i < \theta_c$  and the value one for  $\theta_i > \theta_c$ .

If the photon was reflected by the wrapping the direction  $\vec{d}^*$  which the photon would take if undergoing specular reflection is calculated ( $i\vec{d} = (x, y, z) \rightarrow \vec{d}^* =$

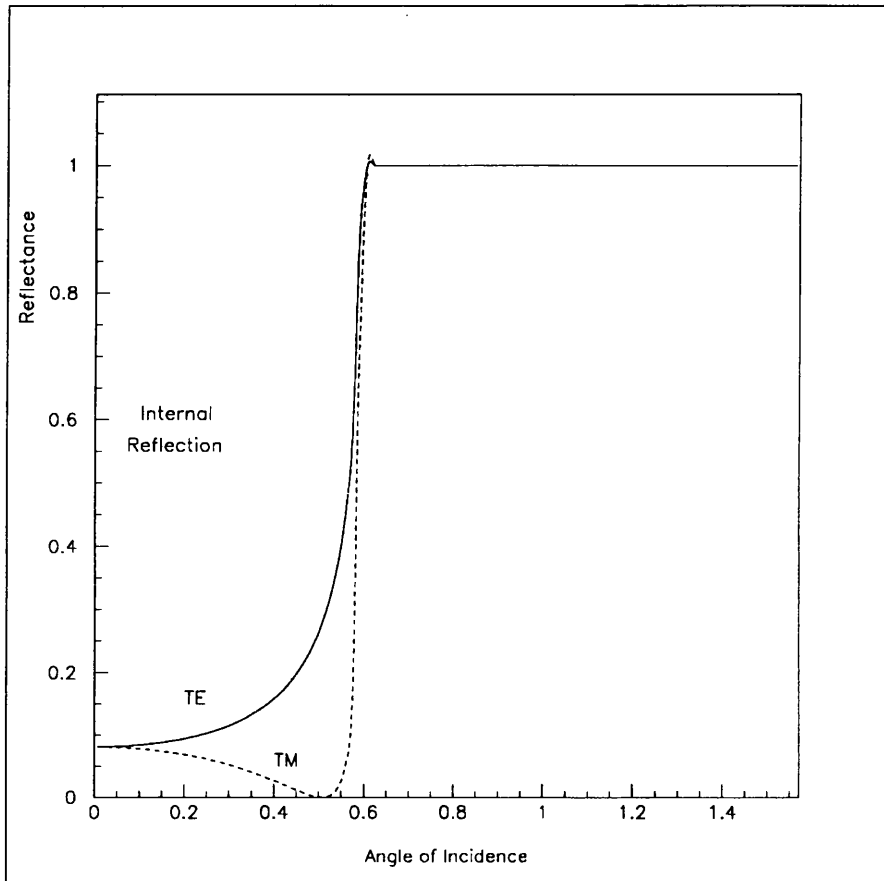


Figure 4.1: *Reflectance function for CsI.*  
The angle of incidence is given in radians

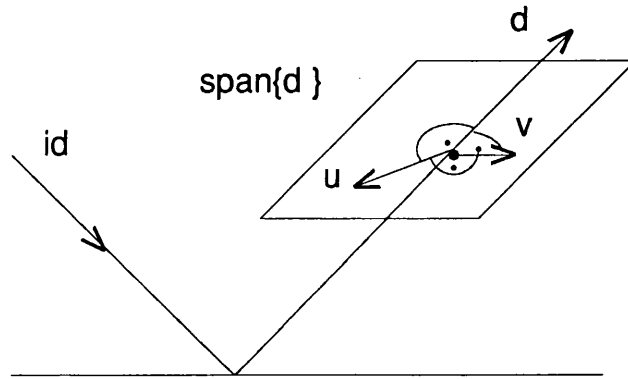


Figure 4.2: *Illustration of the procedure to obtain the new direction of the reflected photon.*

$(x, y, -z)$ ). In order to perturb this direction, a point in a plane perpendicular to  $\vec{d}^*$  (see Figure 4.2) is chosen to give a new direction  $\vec{d}$ . The plane itself is obtained by application of the Gram-Schmidt-Orthogonalization technique (see e.g. [Wo91]) and the selection of the point is weighted by a two-dimensional Gaussian distribution, centered on  $\vec{d}^*$  in this plane. The Gaussian was chosen to have a model in which features of both specular and diffuse reflection are combined and whose relative importance can easily be changed by using different values for the standard deviation  $\sigma$  of the Gaussian; e.g.  $\sigma = 0$  gives specular reflection and the degree of diffuse reflection increases with bigger values for  $\sigma$ . The standard method (also known as the 'Box-Muller-method'; see appendix B) was used to generate the above probability distribution. With this new direction the next point of intersection is determined and the whole process is repeated until the photon is either absorbed inside the crystal, escapes the crystal or enters the diode.

When applying this model one has to take care of one paradoxical situation

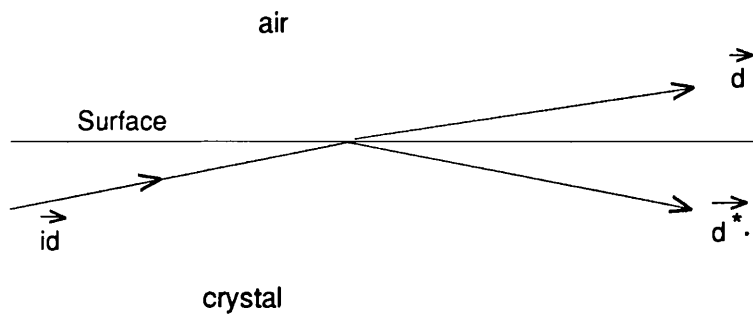


Figure 4.3: *Paradoxical Situation*

that may arise (see Figure 4.3). Assuming incidence from inside the crystal the direction of the reflected photon may point 'outwards' in which case a new direction is chosen until it points 'inwards'.

### 4.1.2 Results

The above models have been used to obtain the light collection efficiencies for different CsI(Tl) crystal sizes read out by different diode sizes. CsI(Tl) has a refractive index  $n$  of 1.8, the reflectivity was set to 0.95 and the attenuation length was assumed to be 1m. No information could be found on the attenuation length of CsI(Tl), however an attenuation length of the order of 1m has typically been assumed [Le87]. The results for the light collection efficiency for different crystal sizes and different diode sizes are shown in Tab. 4.1:

Table 4.1: Light collection efficiency for different crystal and diode sizes

crystal size (diode size)	Lambertian diffuser	Gaussian reflector $\sigma=0$ (specular reflection)	Gaussian reflector $\sigma=0.5$
$5 \times 5 \times 5 \text{ cm}^3$ ( $2.8 \times 2.8 \text{ cm}^2$ )	0.27	0.22	0.21
$5 \times 5 \times 5 \text{ cm}^3$ ( $1.8 \times 1.8 \text{ cm}^2$ )	0.13	0.10	0.09
$5 \times 5 \times 5 \text{ cm}^3$ ( $1.0 \times 2.0 \text{ cm}^2$ )	0.09	0.06	0.06
$2.5 \times 2.5 \times 6 \text{ cm}^3$ ( $1.8 \times 1.8 \text{ cm}^2$ )	0.50	0.37	0.35
$2.5 \times 2.5 \times 6 \text{ cm}^3$ ( $1.0 \times 2.0 \text{ cm}^2$ )	0.32	0.25	0.24
$2.5 \times 2.5 \times 3 \text{ cm}^3$ ( $1.8 \times 1.8 \text{ cm}^2$ )	0.52	0.43	0.39
$2.5 \times 2.5 \times 3 \text{ cm}^3$ ( $1.0 \times 2.0 \text{ cm}^2$ )	0.39	0.30	0.26
$10 \times 50 \times 100 \text{ cm}^3$ ( $10 \times 50 \text{ cm}^2$ )	0.06	0.12	0.12

It is observed that the Gaussian reflector model gives only modest differences to specular reflection, whereas for small crystals higher light collection efficiencies are obtained with the Lambertian diffuser model. This phenomenon can be made plausible by pointing out that a Lambertian diffuser model covers the full range of  $[0, 2\pi]$  for the reflected ray which gives finite probability of 'backscattering' events. The Gaussian reflector model, however, only allows a perturbation of  $[0, \frac{\pm\pi}{2}]$  for the reflected ray relative to the direction resulting from specular reflection, and therefore only takes account of small to medium perturbations relative to specular reflection, dependent on the choice of the value for  $\sigma$ . Using  $\sigma=0.1$ , almost the same light collection efficiencies as for

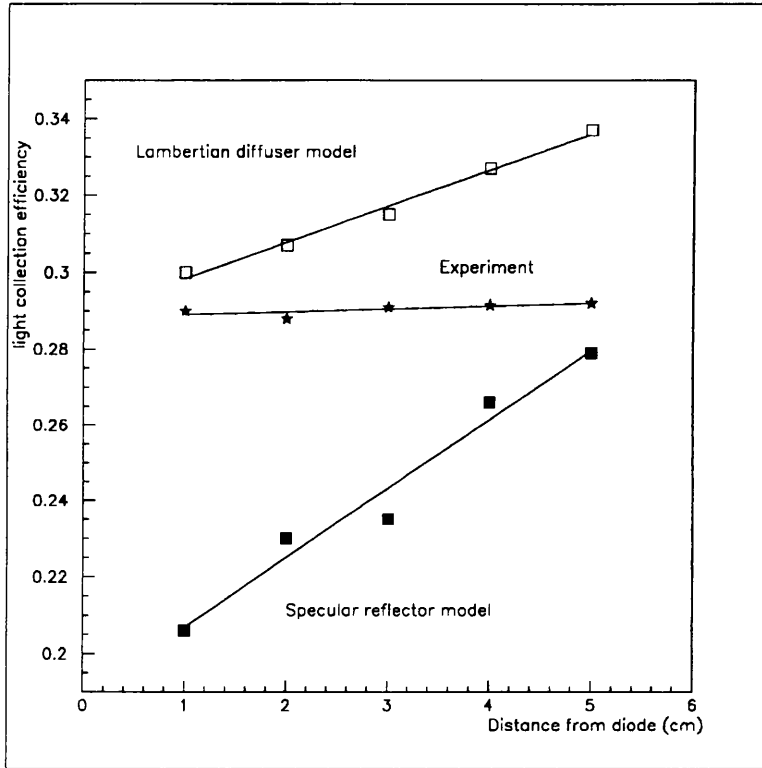


Figure 4.4: *Light collection efficiency for generation of scintillation quanta in different crystal regions.*

Results for the  $25 \times 25 \times 60 \text{mm}^3$  read out by a  $10 \times 20 \text{mm}^2$  diode

specular reflection have been obtained. With the model as it stands values of  $\sigma > 0.5$  require very large amounts of CPU time and thus were not considered. As a check, also a large scintillator has been modelled. The result was that for large crystals the specular reflector model is more efficient than the perfect diffuser model, as one would expect. Both extreme cases - the specular reflector model and the Lambertian diffuser model - have been used to determine the dependence of the light output on the distance from the readout device (which is in our case a photodiode). The dependence found is shown in Figure 4.4.

The tendency is the same for both models. Although it should be noted that diffuse reflectors, whose reflective properties can (depending on the degree of roughness of the surfaces) be viewed as some superposition of these extreme cases, provide a means of reducing the position dependence of the light collection efficiency. In Figure 4.4 the relative deviation from uniformity is  $\sim 25\%$  for the specular reflector compared to  $\sim 12\%$  for the totally diffuse reflector. However, it is clear that the deviation from uniformity found with these models is much larger than the one found in the measurement which was  $\sim 2\%$ .

## 4.2 Simulation of the Proton Detection

To investigate the proton detection characteristics, the GEANT 3.21 [Ge94] package, the detector simulation tool developed by CERN, has been used. GEANT provides useful geometrical tracking packages. The tracking of particles through a detection system is done by taking appropriate physical interactions of the particle with the detector materials into account.

### 4.2.1 Effect and Importance of Proton-Nuclei-Interactions

Examining protons at energies around 40 MeV, it is important to know the number of nuclear interactions it can undergo when it passes through a material.

In our case only inelastic interactions with the nuclei are important. This is due to the fact that

i) elastic scattering is peaked forward resulting in an only mildly perturbed di-

reaction and

ii) the energy transferred to the nucleus in an interaction of this kind is negligible, especially when the scintillation material is a compound of heavy nuclei as is the case for CsI(Tl).

The mechanism of reactions initiated by protons at kinetic energies  $T_p \in [0-50]$  MeV can be divided into 3 regions [Bl52].

- 1) In the low energy region (up to 10 MeV for heavy nuclei) the proton reactions only consist of elastic scattering. The proton energy is too low to penetrate the Coulomb barrier and hence the probability of nuclear effects is negligible.
- 2) In the intermediate energy region the (p,n) reaction becomes dominant.
- 3) If the proton has an energy of a few tens of MeV it may initiate secondary reactions. Frequently the compound nucleus decays by neutron emission but the residual nucleus may have enough energy to de-excite by emitting a second particle. The Coulomb barrier suppresses the emission of a proton and thus the (p,2n) reaction will be the most common reaction, unless shell effects (mainly for light elements) have to be considered.

The probability for nuclear interactions is much smaller than the probability for atomic interactions. This can be seen by comparing the cross-sections for these interactions. For the energy region under consideration the total cross-section for nuclear interactions is about 1 barn, whereas the cross-section for atomic interactions is of the order of 10-100 Mbarn.

GEANT versions up to about 3.15 are not suited for handling nuclear interactions of protons at energies of a few tens of MeV. The package is intended

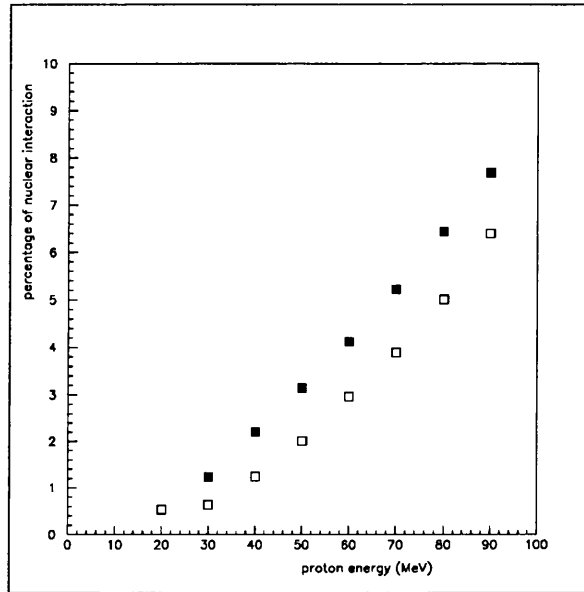
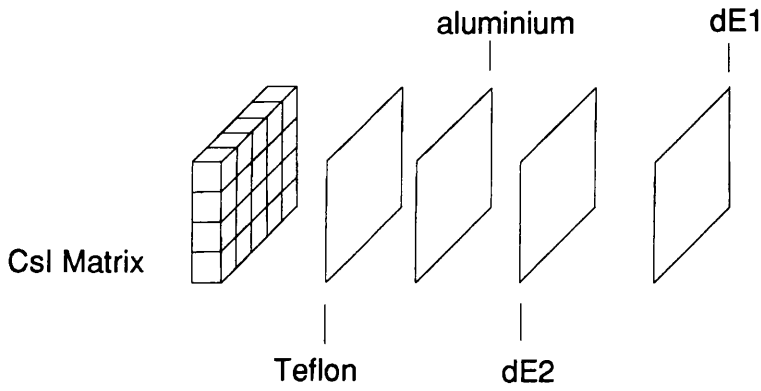


Figure 4.5: *Calculated percentage of nuclear interactions with varying proton energy in CsI*

mainly for use in high-energy physics experiments and so its ability to model processes at such energies is limited. The version of GEANT used (3.21) includes modifications to reproduce the experimentally measured energy deposition of protons in the energy region of interest to us [Pe88].

Figure 4.5 shows the percentage of incident protons in the energy range 10 MeV to 90 MeV which undergo nuclear interactions in CsI, as obtained with GEANT (open squares). Also shown are the values taken from [Me69] (solid squares). The source of the discrepancy between the GEANT values and the values taken from [Me69] lies in the use of different cross sections.

It should be noted that the  $p + \text{Cs}$  and  $p + \text{I}$  cross-section values in the energy range 40-80 MeV are rather uncertain. Measured total reaction cross-sections exist for a limited number of elements, e.g. Ag, Cd and Pb. For these elements the errors are about 5 % and there are several inconsistencies in the data. As



CsI Matrix - Front View

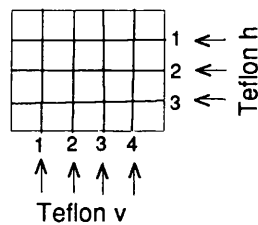


Figure 4.6: *Detector components considered in the present Simulation*

there are no measurements for I and Cs, estimated cross-sections are used by [Me69].

### 4.2.2 Performance of the Detection System

Information about the geometry and composition of the proton telescope (including wrappings), as outlined in chapter 2.2 has been input to GEANT in order to obtain detailed information about energy losses in all the components of the detection system. Figure 4.6 shows the components which have been considered.

In Figure 4.7 the energy losses of 40 MeV protons in the detector components are shown.

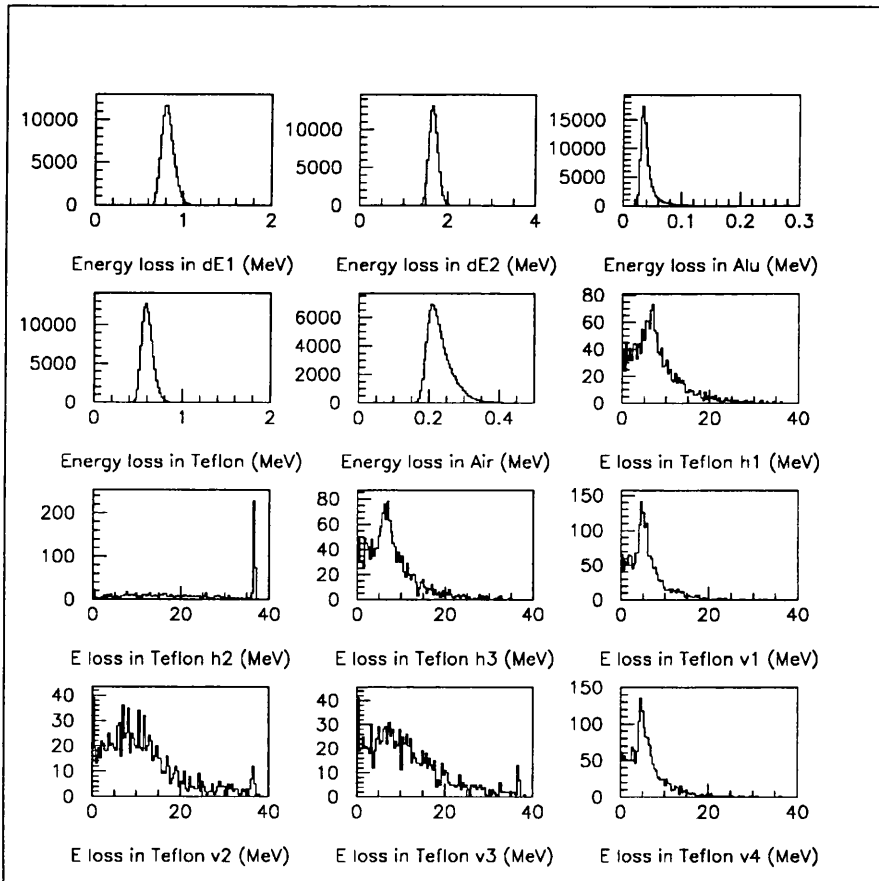


Figure 4.7: Energy losses of 40 MeV protons in various detector components

The mean energy loss in the  $\Delta E$  detectors, aluminium and teflon, i.e the energy loss before the CsI is shown in Figure 4.8. It can be seen that the energy loss in these materials is strongly dependent on the proton kinetic energy. When examining proton energy spectra, the energy-dependent energy loss in these detector components has to be taken into account. The amount of straggling in the  $\Delta E$ 's, aluminium and teflon for proton kinetic energies in the range of 30 to 55 MeV was found to be  $\sim 0.3$  MeV (fwhm) and did not show variations in this range.

Furthermore the energy loss of energetic muons in the CsI blocks has been determined to provide information useful for calibrating the individual CsI crystals. The muons under consideration are generated by interactions of ultra high energy particles (protons, electrons, positrons, alpha particles and other nuclei) in the upper atmosphere.

Although the muons generated by cosmic rays differ in energy, the mean is  $\sim 2$  GeV at sea level and the vast majority of them are minimum ionizing, which means that their mean energy loss per cm in a given medium is a constant.

Muons become minimum ionizing at an energy of  $\sim 300$  MeV [Le87]. Therefore this energy value has been used in GEANT to obtain the energy loss of cosmic ray muons in the CsI(Tl) detectors. The result of this simulation is shown in Figure 4.9.

In this context it is necessary to mention that a point source of muons, placed 20 cm directly in front of the detector array has been used in GEANT, so that there are few events observed where a muon penetrates only a part of an individual crystal. This results in a small background in the region below the peak. Figure 4.10 shows cosmic ray spectra obtained experimentally. In this experiment a large liquid scintillator  $\Delta E$  detector, placed directly above the

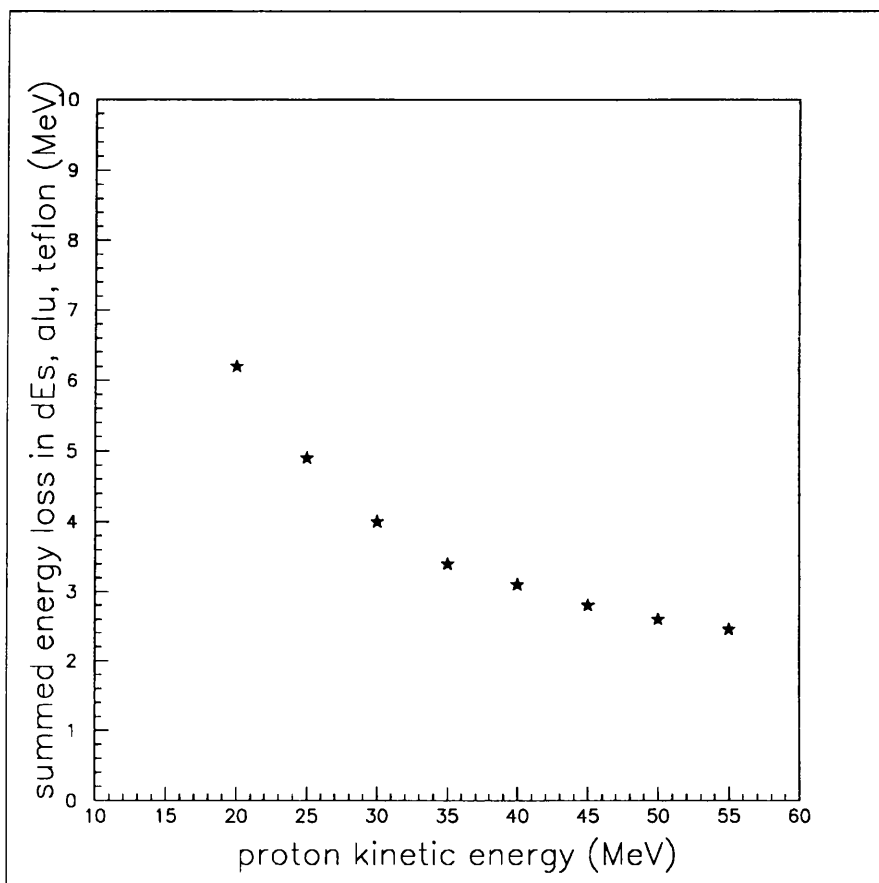


Figure 4.8: *Proton kinetic energy dependent energy loss in the  $\Delta E$  detectors, aluminium and teflon - Simulation*

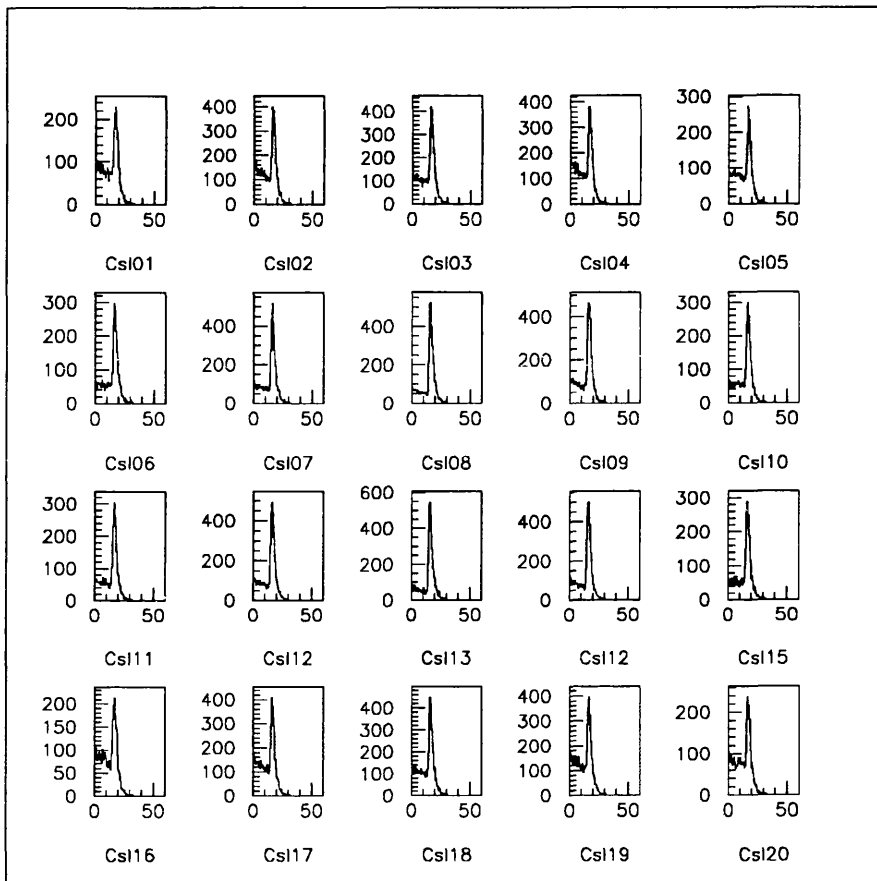


Figure 4.9: Energy losses of 300 MeV muons in the 20 CsI(Tl) blocks - Simulation

The x-axis gives the energy loss in MeV. The peaks are at  $\sim 17$  MeV.

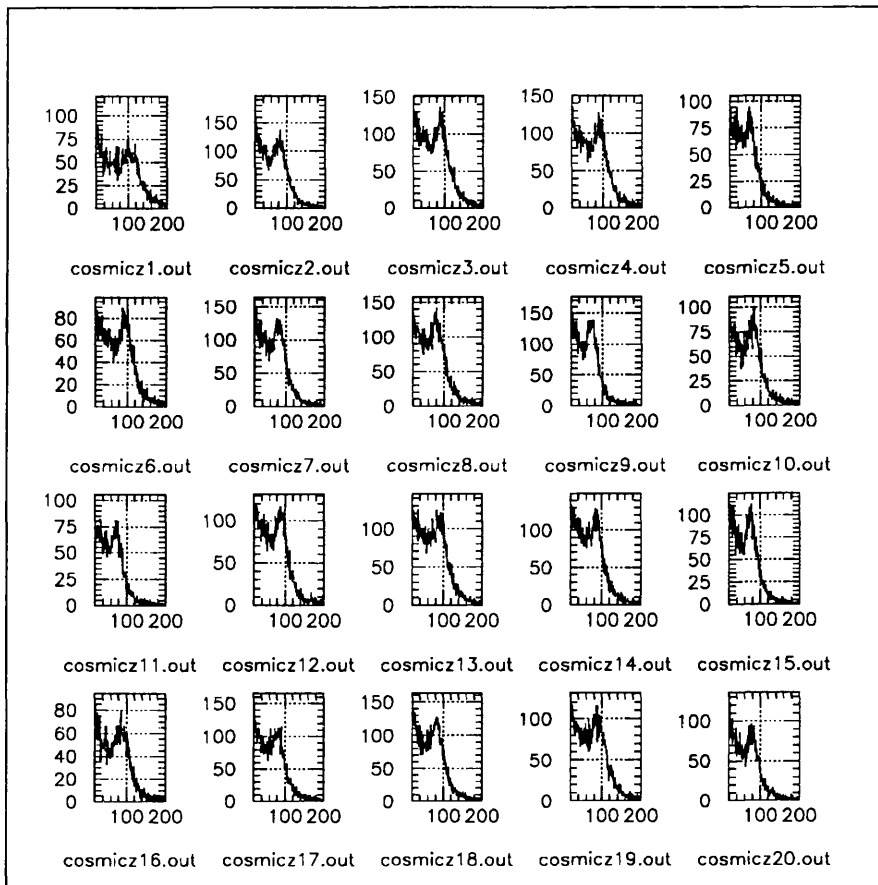


Figure 4.10: *Energy losses of cosmic ray muons in the 20 CsI(Tl) blocks - Experiment*

CsI(Tl) array and covering it completely, was used to trigger the acquisition system. This resulted in having a big deviation from a point source and hence a strong background below the peak, due to events where muons penetrate only a fraction of the crystal, is observed.

## **Chapter 5**

# **Test of the Proton Detector**

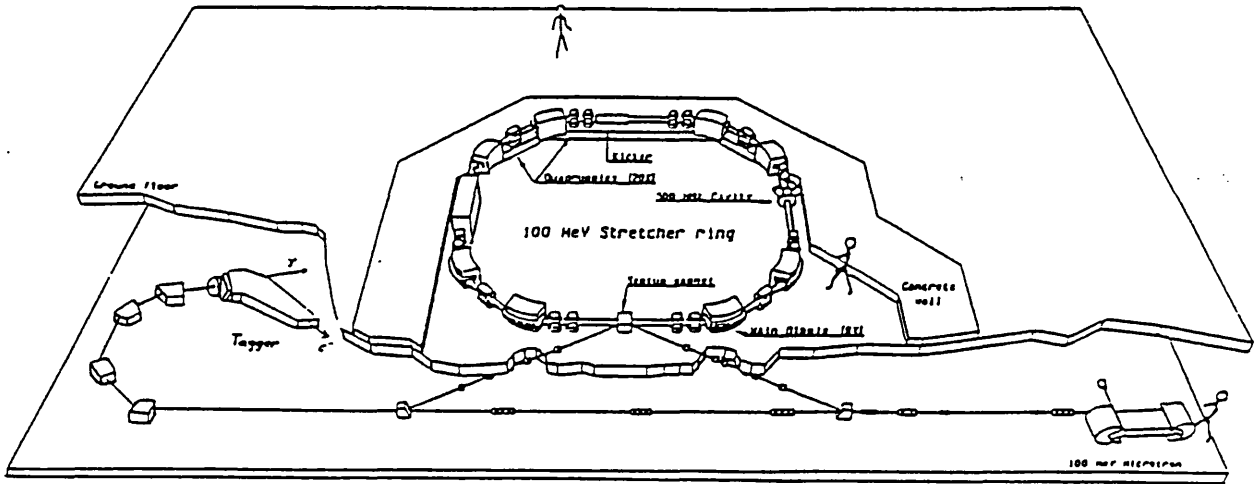


Figure 5.1: *The MAX accelerator in Lund (Sweden).*

Shown is the microtron (bottom right), the stretcher ring (centre) and the tagger in the nuclear physics area (bottom left).

## 5.1 Experimental Setup

The racetrack microtron at MAXLAB, shown in Figure 5.1, is capable of accelerating electrons to a maximum of 100 MeV. In this test run, an energy of 93 MeV has been used. The acceleration of electrons is performed by recirculating the beam through a 5 MeV linear accelerator (linac). This is possible, because  $180^\circ$  turning magnets are employed to feed the linac several times. The operating frequency is  $\sim 50$  Hz. In order to have an almost uniform (i.e. high duty cycle) electron beam available, the pulsed microtron beam is first injected into a pulse stretcher ring before it is used for nuclear physics experiments.

### 5.1.1 Tagged Photons

In the nuclear physics experimental area the stretched electron beam impinges on a  $50\mu\text{m}$  thick aluminium foil (radiator) which serves as a bremsstrahlung converter. Only a small fraction ( $< 0.1\%$ ) of the electrons interact with the aluminium atoms of the radiator to produce bremsstrahlung photons. The tagger dipole transports non-interacting electrons to a beam dump. For interacting electrons the energy of the photons produced via the bremsstrahlung process is simply the difference between electron energy before and after interaction with an aluminium atom. After interaction, the electrons are momentum analyzed in the tagger and their energy is determined by their hit position on the tagger focal plane. The tagging spectrometer basically consists of a quadrupole-dipole spectrometer and a ladder of 64 focal plane detectors (FPD). The magnetic field of the tagging magnet forces the electrons on energy dependent trajectories and hence only electrons with a specific energy (or energy range, because of the finite size of the FPDs) can reach the position of a specific focal plane counter. Thus the index of each FPD is equivalent to a range of electron energies. Since the initial electron energy is known (we use a monoenergetic electron beam), the index of each FPD is also equivalent to a photon energy. Therefore, in order to get the energy of a specific photon which triggered a nuclear reaction in the reaction target, where a particle is emitted and detected, we only have to look at the relative timing of the FPDs and the particle detector. The index of the FPD time to digital convertor (TDC) which has a count in coincidence with an event in the particle detector determines the photon energy, i.e. the photon is energy tagged. This is illustrated schematically in Figure 5.2.

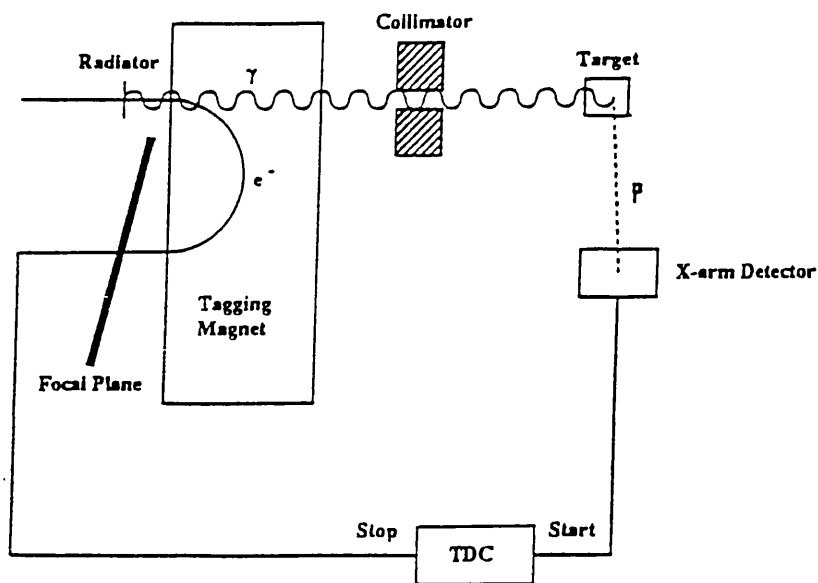


Figure 5.2: *Schematic diagram of the tagging technique*

In the test described here, photons were energy tagged in the range between 49.4-58.9 MeV and 60.4-70.2 MeV. The width of the FPDs determines the energy resolution of the tagger which is  $\sim 0.30$  MeV. The tagging efficiency, i.e. the number of photons incident on the target per energy interval, divided by the number of electrons in the focal plane scintillator defining that interval, was about  $\sim 25\%$ . This means that only one out of four photons could pass the collimation system. The collimation system basically consists of two collimators and a magnet. The function of the first collimator is to keep the beam diameter small. Since this produces low energy electrons and positrons, a sweeping magnet and a second, larger-aperture collimator located downstream of the first are needed.

### 5.1.2 Target

The target employed was a sheet of graphite. Its thickness determines the number of events per time interval and, due to different path lengths inside the target, also the energy spread of the protons. Therefore, the optimum target thickness is a compromise between counting rate and energy resolution. In the May test run, a thickness of  $118 \text{ mg}\cdot\text{cm}^{-2}$  was chosen which corresponded to an energy spread of  $\sim 1.4 \text{ MeV}$  for the protons of  $\sim 40 \text{ MeV}$  under investigation. In the actual experimental run in June, a target thickness of  $235 \text{ mg}\cdot\text{cm}^{-2}$  was used which corresponded to an energy spread of  $\sim 2.9 \text{ MeV}$  for  $40 \text{ MeV}$  protons.

### 5.1.3 Electronics

Figure 5.3 shows the electronics used in the  $^{12}\text{C}(\gamma, p\gamma')^{11}\text{B}$  experiment. The picture shows the electronics which are necessary to obtain the CsI pulse height spectra, the energy of the photon which initiated the emission of the proton and the energy of the de-excitation  $\gamma$ 's.

The following gives a short description of the signal processing. Coincident pulses in both  $\Delta E$  detectors above certain thresholds, which are adjusted in the corresponding CFDs, are required in order to obtain gates for the CsI ADCs and to initiate the data readout. In this way, the two  $\Delta E$  detectors form the trigger of the assembly. In case of the rear  $\Delta E$  detector (dE 2) the sum of both PM signals is given to a CFD, to account for position dependence of the pulse height. The requirement that dE 1 and dE 2 have to have a pulse above certain thresholds is accounted for by using a logic AND gate, which only gives

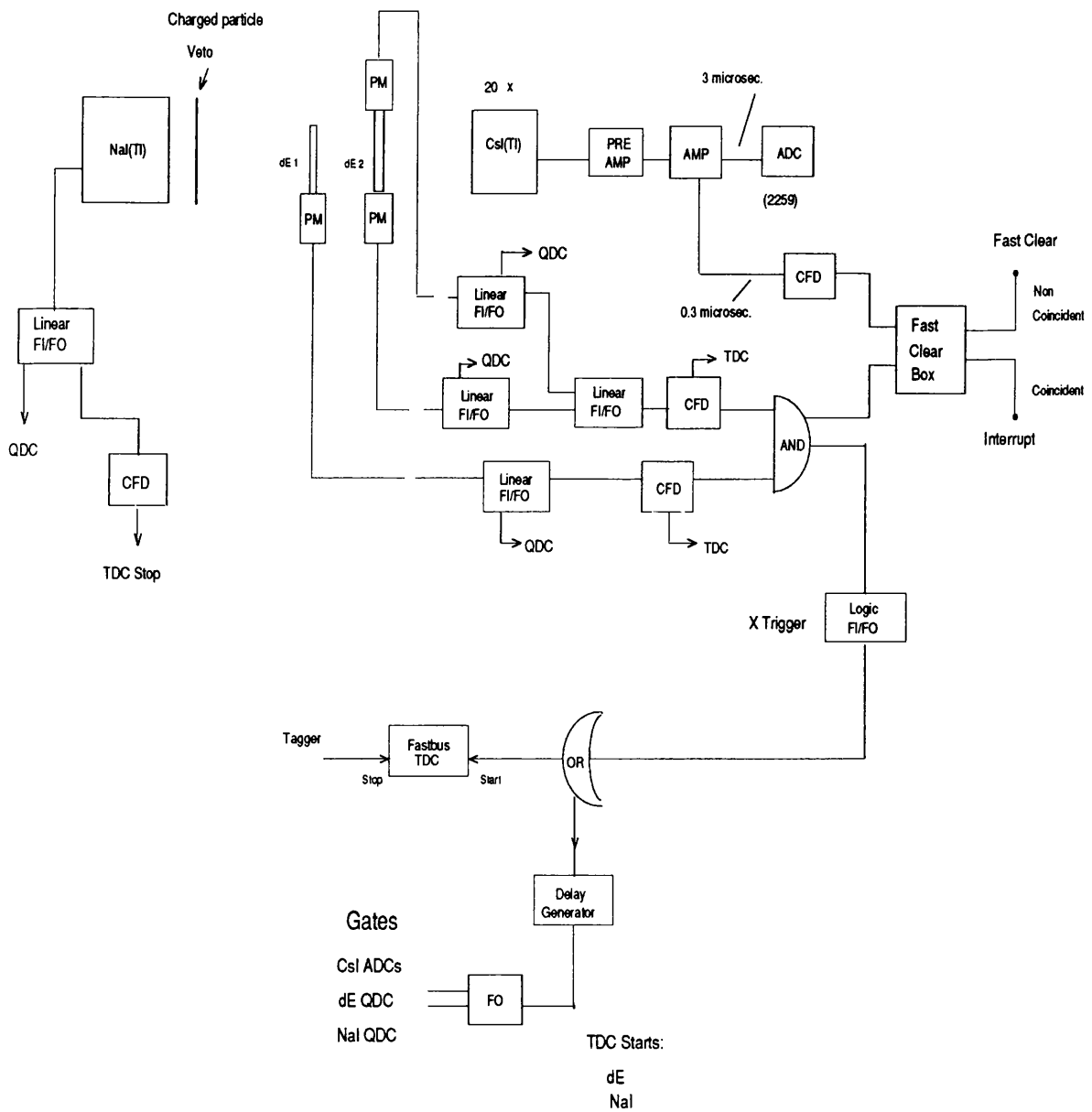


Figure 5.3: Schematic diagram. Electronics for signal processing related to the proton detection system.

an output if the inputs come in coincidence. If a coincident signal in both  $\Delta E$  detectors was present all ADCs are gated and the TDCs including the 64 FASTBUS TDCs are started. Each individual FPD is coupled to an individual TDC. The index of the TDC which shows a time coincidence between the  $\Delta E$ s and its corresponding FPD determines the photon energy<sup>1</sup>. The advantage of taking the timing signals from the  $\Delta E$ s rather than from the CsI signals is that a much better timing resolution ( $\sim 1$ ns) can be achieved. The main reason for this is the relatively long decay time of CsI(Tl) scintillator ( $\sim 1\mu$ s).

Also shown in Figure 5.3 is a FAST CLEAR circuit which has been installed to reduce the dead time of the system generated by unwanted triggers, mainly stemming from low energy electrons detected in the  $\Delta E, E$  telescope. The processing of events is the main source of dead time in the experiment. This is because during the rather time consuming process of the computer readout of the ADC and TDC contents, which takes  $\sim 1$  ms, a latch arrangement disables further triggers. Therefore, the use of a fast ( $0.3\mu$ s integration time) CsI amplifier output (see Chapter 2.3), which allows the rejection of events below a minimum energy, is an effective way to increase the live time. Effectively a coincidence between CsI and  $\Delta E$ 's is demanded for an interrupt. If there is no such coincidence, the FAST CLEAR is applied.

## 5.2 Missing Energy Spectra

As a test of the performance of the proton detector, the data which was recorded in a  $^{12}\text{C}(\gamma, p)$  test run at MAXLAB in May and June 1995 has been analyzed

---

<sup>1</sup>It is possible that more than one of the FPDs meets the coincidence condition ( $\rightarrow$  multiple hits)

to produce the missing energy of the reaction. This should show peaks corresponding to the excitation of discrete states in  $^{11}\text{B}$ . The widths of these peaks result from

- photon energy resolution
- CsI energy resolution
- target thickness
- angle uncertainty (small)

For  $(\gamma, p)$  reactions the missing energy  $E_m$  is the photon energy less the kinetic energies of the emitted proton and recoil nucleus. Therefore, in order to obtain missing energy spectra the following quantities have to be measured

- the proton kinetic energy
- the photon energy
- the emission angle  $\theta_p$  of the proton

Once this has been done, the calculation of the missing energy  $E_m$  can be performed using the formula

$$E_m = \sqrt{(E_\gamma + M_t - E_p)^2 - (E_\gamma^2 + p_p^2 - 2E_\gamma p_p \cos(\theta_p))} + M_p - M_t$$

The indices p, t and  $\gamma$  stand for proton, target and photon, respectively. The proton emission angle  $\theta_p$  is the angle between the photon and proton momentum vectors and its determination is straightforward. Since the E detector is segmented into small blocks (CsI matrix), simple geometrical considerations can be used to get the mean angle for each block. Although there might be applications where a more accurate determination of this quantity is necessary, in the test described here the use of an average angle is sufficient. This is because with a relatively massive target small uncertainties (a few degrees) of  $\theta_p$  have only a small influence on the missing energy  $E_m$ .

The following will describe how the kinetic energy of the proton and photon have been obtained from the data collected in the runs.

If not fast cleared, each trigger during an experimental run initiated the storage of all ADC and TDC contents as an event. In order to focus the analysis, only those events where a proton gave the trigger the original data were recorded event by event and then analyzed off-line. Selection of protons was made by applying region (or polygon) cuts on all  $\Delta E$ -E scatter plots, which was easy because a well defined proton locus allowed a clear separation of proton events from non-proton (mainly electron) events to be made (see Figure 2.1). The events which passed the cut were written to an output file for further analysis. The analysis of these reduced data files, which contained a factor of  $\sim 10$  less data than the originals, was also done event by event. It started with the determination of the CsI blocks which showed energy above a required minimum and was done by looping around all the corresponding ADCs, thereby picking

out those ones which had a count above a software imposed limit, after the pedestal channel number (i.e. the ADC channel number which corresponds to zero energy) had been subtracted. For those ADCs the proton emission angle  $\theta_p$  was looked up in a table and using a previous calibration (see Chapter 4.2.2) the conversion from channel number to energy was performed. Correction was then made for energy-dependent energy losses of protons in the  $\Delta E$  detectors. The  $\Delta E$  energy losses were tabulated using values taken from a GEANT simulation which gave values in steps of 5 MeV for the initial proton energy, and the actual energy correction was iteratively performed using interpolation to obtain values between the tabulated points.

The next step was to find the energy of the photon which initialized the proton emission. This was done by looping around all the ladder time spectra, picking out those ones where the time fell within software-defined time windows. Figure 5.4 shows a typical coincidence time spectrum after the data files had been reduced by scatter-plot selection; a rough timing cut was also made. The windows were chosen to select correlated tagger -  $\Delta E$ , E telescope counts and thus the accepted channel position had to lie in the tagging peak of the corresponding TDC<sup>2</sup>.

Having filtered out the 'good' TDCs, a conversion from TDC number ( $\equiv$  ladder element number) to photon energy was made.

Finally for *all* 'good' CsI blocks (i.e. those who had a count above the pedestal position) the missing energy was calculated for *all* photon energies, whose corresponding TDCs met the condition described above. This means that the analysis can handle events where the multiplicities of the CsI and the tagger

---

<sup>2</sup>After the region cuts on proton events all the ladder TDC spectra showed a clear peak stemming from correlated stops.

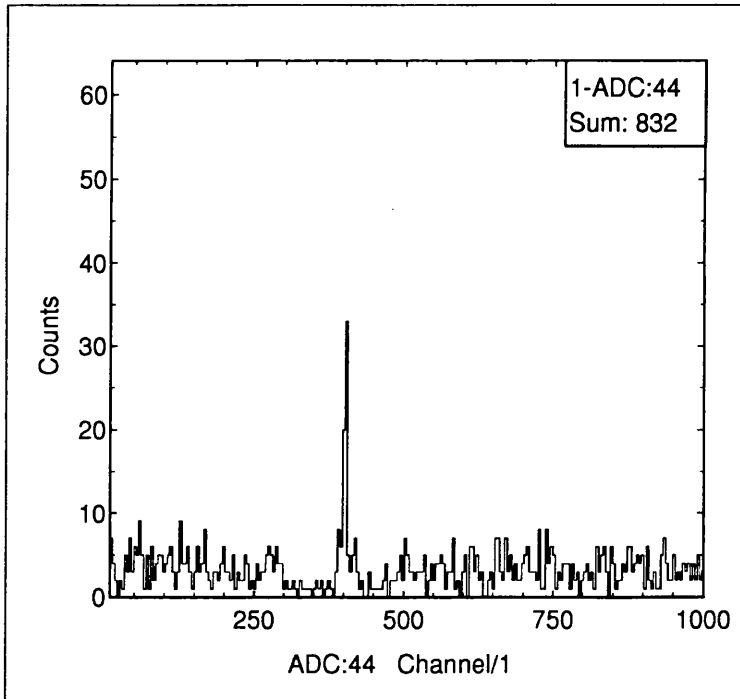


Figure 5.4: *Typical TDC spectrum after scatter-plot proton identification and a rough timing cut*

are greater than one.

Figure 5.5 shows a typical missing energy spectrum obtained in this way (using a preliminary calibration). Due to a lack of counts, it is only possible to identify the ground state and the excited state at 2.1 MeV in  $^{11}\text{B}$ .

### 5.3 Preliminary Results

The following will give a short summary of the results obtained from a quick analysis of the production run in June.

#### Graphite Target

Figure 5.6 shows a NaI  $\gamma$ -spectrum with all events where data readout was trig-

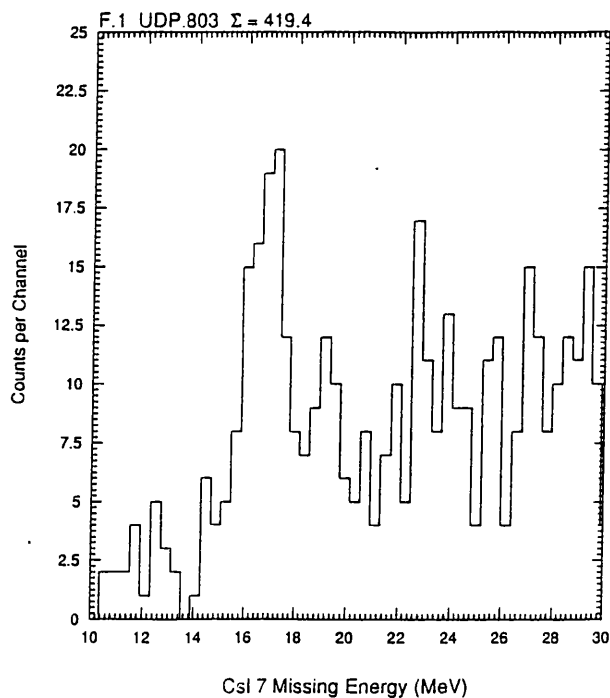


Figure 5.5:  $^{12}\text{C}$  missing energy spectrum. Target thickness  $118\text{ mg}\cdot\text{cm}^{-2}$ . Preliminary calibration.

gered contributing. In order to focus the analysis, the procedure described in the previous chapter was carried out. Figure 5.7 shows some missing energy spectra obtained in this way.

As described in chapter 1, the aim of the experiment is to find out which of the states around 7 MeV excitation energy in  $^{11}\text{B}$  is dominantly populated. Therefore cuts on the missing energy spectra were made, so that only events which contributed to an excitation in  $^{11}\text{B}$  between  $\sim 4\text{--}10\text{ MeV}$  were selected. The main reason why such a relatively big energy range had to be taken emerges from poor energy resolution due to target thickness ( $235\text{ mg}\cdot\text{cm}^{-2}$ ). Figure 5.8 shows some missing energy spectra after the cuts had been made and Figure 5.9 shows the corresponding NaI  $\gamma$ -spectrum. In Figure 5.9 only events which gave entries in Figure 5.8 are contributing. It can be seen that the

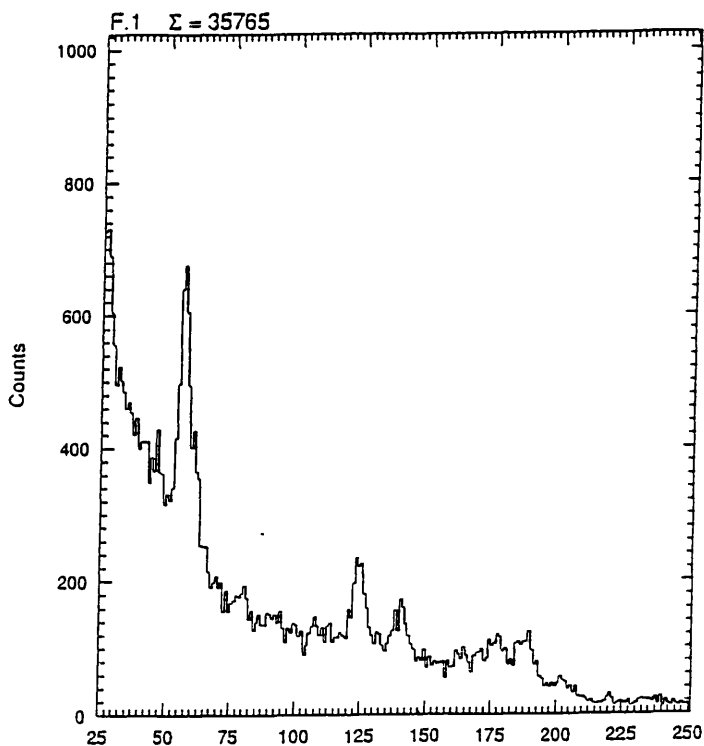


Figure 5.6: Graphite target. NaI  $\gamma$ -spectrum with no conditions applied.

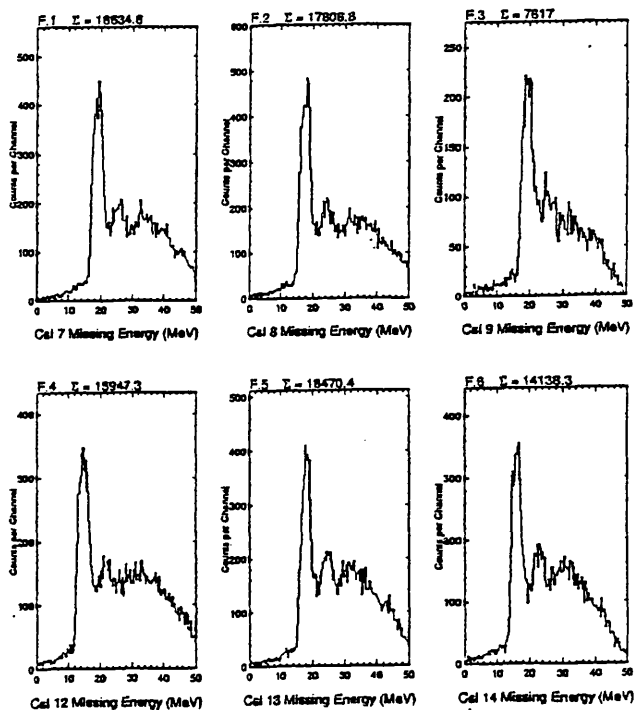


Figure 5.7:  $^{12}\text{C}$  missing energy spectra. Target thickness  $235 \text{ mg}\cdot\text{cm}^{-2}$

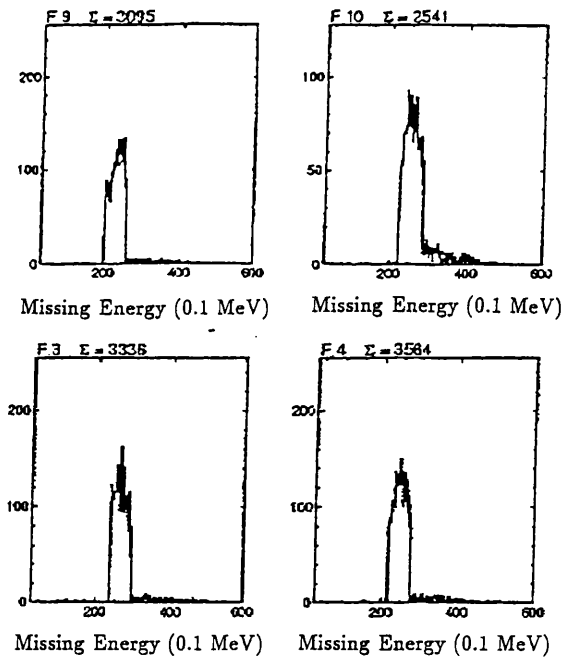


Figure 5.8: *Cuts on missing energy spectra.*

dominant part of the excitation at  $\sim 7$  MeV is due to the doublet of states at  $\sim 6.8$  MeV. A more detailed analysis of the  $\gamma$  ray lines where the  $\sim 7$  MeV states do not decay directly to the  $^{11}\text{B}$  ground state might be able to discriminate which of the states in this doublet is mainly populated.

### Water Target

In order to have a consistency check, a small part of the beam time in June 95 was used to perform  $^{16}\text{O}(\gamma, p\gamma')$ . Thick water targets with thin mylar walls were employed. Figure 5.10 shows the corresponding NaI  $\gamma$ -spectrum after selection of proton events in the CsI's had been made. Figure 5.11 shows the missing energy spectra obtained from this reaction. In Figure 5.10 the peak at  $\sim 5.9$  MeV is totally unexpected, as there are no known excited states in  $^{15}\text{N}$  or  $^{14}\text{N}$  which could give rise to the observation of this  $\gamma$ . The origin of this  $\gamma$  from the target frame holder, the mylar walls or water impurities can be excluded.

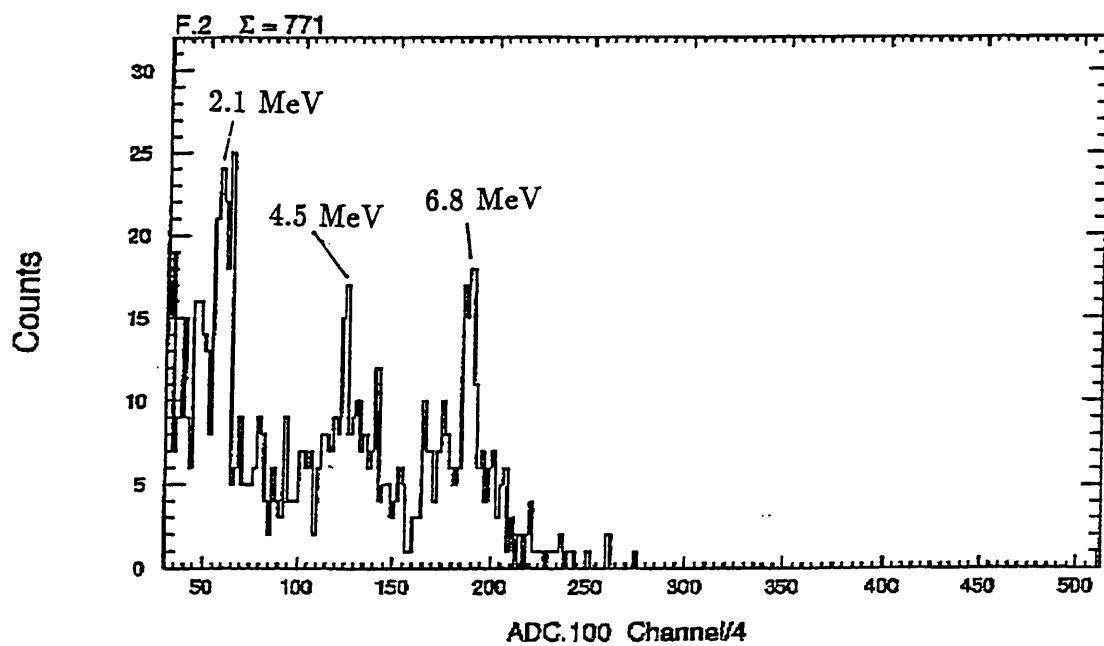


Figure 5.9: Graphite target. NaI  $\gamma$ -spectrum after application of conditions.

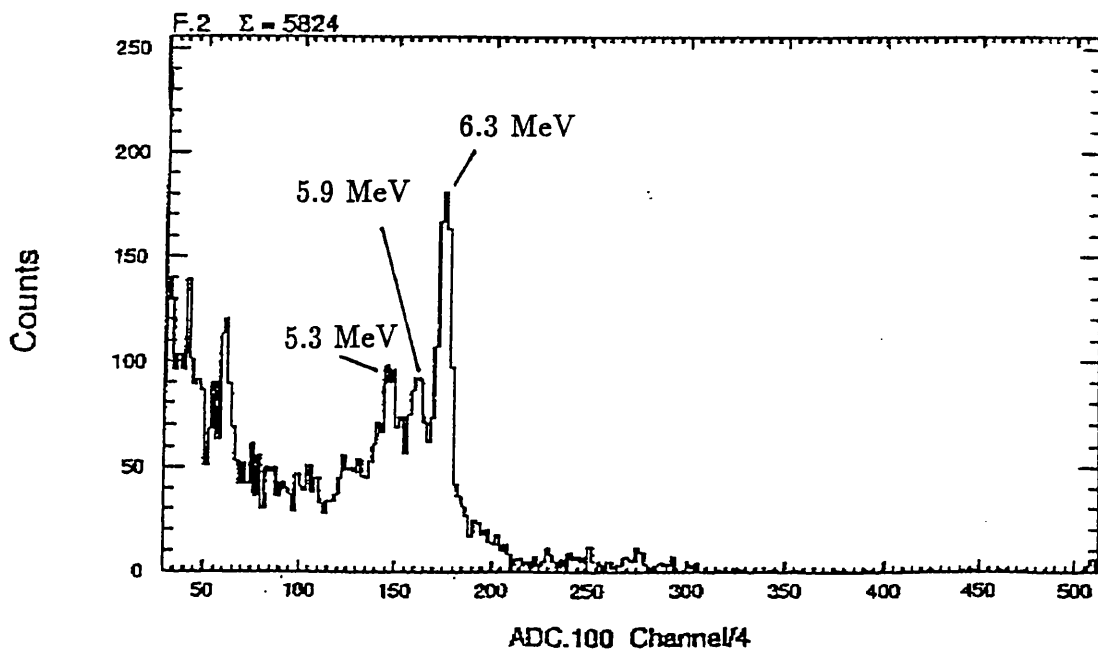


Figure 5.10: Water target. NaI  $\gamma$ -spectrum after selection of proton events.

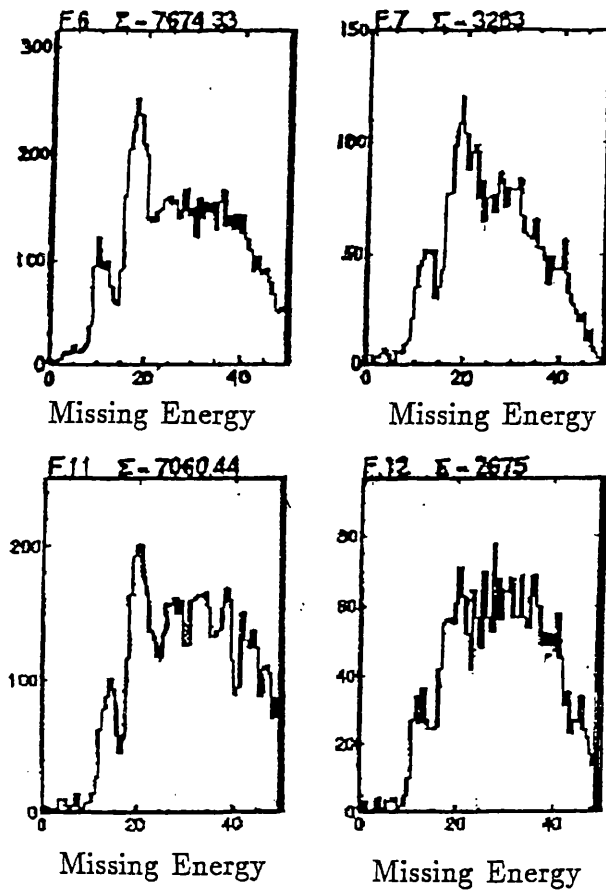


Figure 5.11:  $^{16}\text{O}$  missing energy spectra.

## 5.4 Conclusion

This work has been concerned with a charged particle detector used in a measurement of the  $^{12}\text{C}(\gamma, p\gamma)^{11}\text{B}$  reaction. In order to obtain optimum and predictable detection performance, test measurements and Monte Carlo simulations were made.

Experiments which use the tagged photon technique were carried out with this detector at MAXLAB, University of Lund (Sweden). The results of a quick preliminary analysis of the experiments show that the detector matrix is working properly and with adequate resolution to separate discrete excited states in the residual nucleus ( $^{11}\text{B}$ ). The energy resolution of the detector was not dominant in the overall energy resolution, which was mainly due to target thickness.

The technique of using proton detectors as triggers for data readout in combination with efficient  $\gamma$ -detectors to give the energy of the excited states of the residual nucleus was shown to be feasible. In addition, it was shown that setting windows on certain ranges of missing energy is an efficient way of reducing background in the  $\gamma$  detectors.

# **Appendix A**

## **The Bethe-Bloch Equation**

In order to obtain the energy loss of charged particles (heavier than the electron) in matter one makes use of the standard quantum-mechanical formula, the Bethe-Bloch formula. The derivation of this equation assumes that the absorber electrons are free and initially at rest, the interaction is thought to happen instantaneously. The validity of this equation is limited to particles heavier than the electron, because no flight path deviation due to interaction processes is considered. When taking account for the density effect correction  $\delta$  and the shell correction C, then the formula (in SI units) obtained is [Le87]

$$\frac{dE}{dx} = 4\pi N_A r_e^2 m_e c^2 \rho \frac{Z Z_p^2}{A \beta^2} \left[ \ln\left(\frac{\gamma \beta c \sqrt{2m_e W_{max}}}{I}\right) - \beta^2 - \frac{\delta}{2} - \frac{C_e}{Z} \right]$$

with

$$W_{max} = \frac{2m_e c^2 (\gamma^2 - 1)}{1 + 2\frac{m_e}{M} \sqrt{1 + (\gamma^2 - 1)} + \left(\frac{m_e}{M}\right)^2}$$

A	mass number of medium
Z	atomic number of medium
$r_e$	$2.8 \cdot 10^{-15} \text{m}$
	classical electron radius
$m_e$	electron mass
$\rho$	density of medium
$Z_p$	charge of particle (units of e)
$\beta$	$\frac{v}{c}$
$\gamma$	$\frac{1}{\sqrt{1-\beta^2}}$
C	shell correction
$W_{max}$	maximum energy transfer in a single collision
$N_A$	Avogadro's number
I	mean excitation potential

Values for I can be obtained by using semi-empirical formulas, like

$$\frac{I}{Z} = 12 + \frac{7}{Z} eV \quad Z < 13$$

$$\frac{I}{Z} = 9.76 + 58.8 Z^{-1.19} eV \quad Z \geq 13$$

The shell and density corrections, i.e. the quantities  $\delta$  and  $C$  are not important for the energies under consideration in this Thesis. However, they have to be taken into account at high ( $\geq 1$  GeV) and low energies ( $< 1$  MeV).

The reason for the necessity of density corrections is that the electric field of the particle polarizes the atoms along its trajectory, and therefore electrons at greater distance feel only a reduced electric field intensity (shielding effect). Since the induced polarization is bigger in condensed materials than in fluids or gases, the term density effect was chosen.

The shell correction has to be made if the particle velocity is of the same order as the orbital velocity of bound electrons. In this case the absorber electrons cannot be viewed as stationary with respect to the particle.

## **Appendix B**

# **Generation of Non-Uniform Probability Distributions**

Let  $r$  denote a uniformly distributed random number in the unit interval  $[0,1]$ , i.e. its probability density function  $p(r)$  is defined by

$$p(r) = \begin{cases} 1 & , \quad r \in [0, 1] \\ 0 & , \quad otherwise \end{cases}$$

The aim is to obtain a random number  $x$  which is distributed according to  $p(x)$ . One important method to achieve this is to find a relation  $x(r)$  that transforms the uniform distribution to the desired one.

It is assumed that  $p(x)$  is normalized to one,

$$\int_{-\infty}^{+\infty} dx p(x) = 1.$$

By defining the function

$$P(x) = \int_{-\infty}^x dx' p(x'),$$

the probability of obtaining a number less than or equal to  $x$  and setting

$$P(x) = r,$$

one has determined  $x$  as a function of  $r$ . If it is possible to perform the integral - analytically or numerically - and if it is possible to invert the latter equation, then the determination is unique and the desired solution is immediately found as

$$x = P^{-1}(r).$$

It is evident that  $x$  is distributed according to the probability function  $p(x)$  when looking at

$$dP(x) = p(x)dx = p(r)dr.$$

The above method is called the **inverse transformation method** and generalizes to  $n$  dimensions, where joint probabilities are under consideration. In

n dimensions, the formula which rules the transformation of joint probabilities can be written as

$$p(\vec{y})dy_1dy_2\dots dy_n = p(\vec{x}) \left| \frac{\partial \vec{x}}{\partial \vec{y}} \right| dy_1dy_2\dots dy_n,$$

where  $\left| \frac{\partial \vec{x}}{\partial \vec{y}} \right|$  denotes the Jacobian determinant. [Of course,  $\vec{x}$  and  $\vec{y}$  must be vectors in spaces of equal dimensions]

The Gaussian or normal distribution

$$p(y) = \frac{1}{\sqrt{2\pi}\sigma} e^{-\frac{y^2}{2\sigma^2}}$$

is an example of a probability distribution for which P(y) cannot be obtained analytically. However, it is possible to generate the Gaussian distribution in two dimensions

$$p(y_1, y_2) = \frac{1}{2\pi\sigma^2} e^{-\frac{(y_1^2+y_2^2)}{2\sigma^2}}$$

Making a change to generalized planar polar co-ordinates

$$\begin{aligned} \rho &= \frac{1}{2\sigma^2}(y_1^2 + y_2^2) \\ \theta &= \frac{1}{2\pi\sigma^2} \arctan \frac{y_2}{y_1} \end{aligned}$$

the two-dimensional normal distribution writes

$$p(\rho, \theta)d\rho d\theta = e^{-\rho}d\rho d\theta$$

In order to obtain the cumulative distribution function P( $\rho, \theta$ ) one has to perform the double integral

$$P(\rho, \theta) = \int_0^\rho \int_0^\theta e^{-\rho'} d\rho' d\theta'$$

which gives

$$P(\theta, \rho) = \theta(1 - e^{-\rho})$$

Since  $P(\rho, \theta)$  factorizes into  $P(\rho, \theta) = P_1(\rho) P_2(\theta)$ ,  $\rho$  and  $\theta$  can be generated independently, resulting in  $\rho = -\ln(1-r) = -\ln(r)$  [the uniform random number  $r$  in the unit interval has the same distribution as  $1 - r$ ] and  $\theta = r$ .

The desired functions for the generation of  $y_1$  and  $y_2$  hence are

$$y_1 = \sqrt{-2\sigma^2 \ln(r)} \cos(2\pi\sigma^2 r)$$

$$y_2 = \sqrt{-2\sigma^2 \ln(r)} \sin(2\pi\sigma^2 r)$$

The above process is known as the 'Box-Muller method'.

# Bibliography

[An93] J. ANNAND ET AL.: ACQU Manual

[Ar81] ARENHÖVEL (ED): From collective states to Quarks in Nuclei (Springer, Berlin, 1981) p.171

[Be94] J.BEA ET AL.: Simulation of light collection in scintillators with rough surfaces, NIM A 350 (1994) 184-191

[Bl52] BLATT, WEISSKOPF: Theoretical Nuclear Physics (Wiley, New York, 1952) p.484-496

[Ca84] M. CAVATINO ET AL.: Nuclear Physics A422, 237 (1984)

[De69] C.F.G. DELANEY: Electronics for the physicist (Penguin, London, 1969) p.245-248

- [Ga93] CARL GAARDE:  $\Delta$ -isobars in nuclei; vol.3,no2, 1993,Nuclear Physics News p.17ff
- [Ga81] M. Gari and H. Hebach, Phys Rep 72 (1981) 1
- [Ge94] Geant 3.21, CERN Data Handling Division (Geneva, 1994)
- [Gr88] GRASSMANN ET AL.: Results from a CsI(Tl) test calorimeter with photodiode readout between 1 and 20 GeV, NIM A235 (1985) 319-325
- [Ha94] HAMAMATSU: Large-Area PIN Silicon Photodiodes (Technical Data Sheet)
- [He94] K. HEYDE: Basic ideas and concepts in nuclear physics (IOP Publishing Ltd, 1994)
- [Kn79] G.KNOLL: Radiation detection and Measurement, p.651 (John Wiley & Sons, Inc, New York 1979)
- [Ko93] KOTTHAUS: CsI(Tl)-photodiode detectors for spectroscopy at low radiation levels, NIM A329 (1993) 433-439

- [LC92] LECROY: HQV800 Series, 8-channel FET Preamplifiers (Technical Data Sheet)
- [Le87] W.R. LEO: Techniques for Nuclear and Particle Physics Experiments (Springer, Berlin, 1987)
- [Me69] MEASDAY, RICHARD-SERRE: Loss of protons by nuclear interactions in various materials (Geneva, 1969)
- [Ni90] D. NILSSON, PhD Thesis, University of Lund 1990
- [Pe88] P. PEDRONI: INFN/BE-88/3
- [Sh74] DE SHALIT, FESHBACH: Theoretical Nuclear Physics, Volume I: Nuclear Structure, p.709ff (John Wiley & Sons, Inc, New York 1974)
- [Ry88] J. RYCKEBUSCH ET AL.: Nuclear Physics A476, 237 (1988)
- [Wo91] C. WA WONG: Introduction to mathematical physics, p.175f (Oxford University Press, 1991)

